J. Fluid Mech. (2025), *vol.* 1017, A36, doi:10.1017/jfm.2025.10475

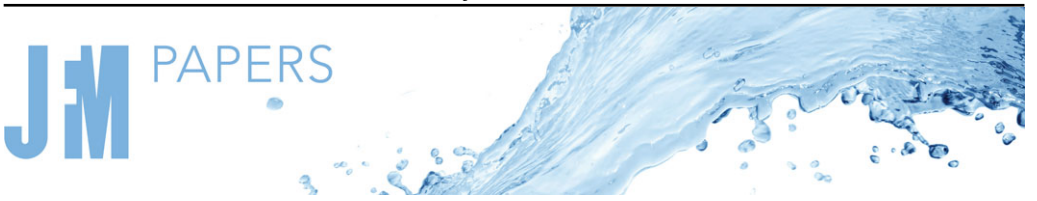

Self-preservation scaling of turbulence in free axisymmetric compressible jets

Kenneth Yi-Nian Hinh, Robert J. Martinuzzi and Craig T. Johansen

Department of Mechanical and Manufacturing Engineering, University of Calgary, 2500 University Drive NW, Calgary, Alberta T2N 1N4, Canada

Corresponding author: Robert J. Martinuzzi, rmartinu@ucalgary.ca

(Received 5 February 2025; revised 9 June 2025; accepted 9 July 2025)

The influence of compressibility on shear flow turbulence is investigated within a self-preservation framework. This study focuses on the axisymmetric jet to examine compressibility effects in a slowly spatially evolving flow, unlike mixing layers, where the convective Mach number remains constant. Revisiting self-preservation, an *a priori* description of the compressible scaling for Reynolds stresses and higher-order velocity moments is developed. Turbulence moments are found to scale with powers of the spreading rate, suggesting Reynolds stress anisotropy results from compressibility effects consistent with self-preservation of the governing equations. Particle image velocimetry measurements for Mach 0.3 and perfectly expanded Mach 1.25 jets confirm the scaling predictions. The attenuation function, $\Phi(M_c)$, describing the relationship between the convective Mach number, M_c, and the spreading rate, follows a similar trend in jets and mixing layers, where a higher M_c results in reduced spreading rates. In the jet where M_c decays, the relationship between the local M_c and turbulence attenuation remains captured through $\Phi(M_c)$, which scales proportionally with the spreading rate. A new scale is introduced, where the pressure in the mean momentum equation is substituted. The difference between the streamwise and radial-Reynolds-normal stresses was found to be a scale which is independent of Mach number and spreading rate. Further analysis of the Reynolds-stress-transport budget shows that internal redistribution of energy occurs within the Reynolds-normal stresses, and the role of pressure modification in turbulence attenuation supports previous observations. These findings confirm that the compressible axisymmetric jet exhibits self-preservation, with scaling extending into supersonic regimes.

Key words: jets, compressible turbulence, shear layer turbulence

1. Introduction

Studies of compressible shear layers have focused on the influence of Mach number, M, on turbulence. Early experimental studies of planar mixing layers revealed an inverse relationship between the spreading rate, b', and M (Bradshaw 1977). To characterise these effects, Bogdanoff (1983) introduced the convective Mach number, M_c, suggesting these effects can be scaled by the Mach number difference of the two sides of the shear layer. The reduction in b' is attributed to a reduction of mixing due to the attenuation of turbulence intensity (Vreman, Sandham & Luo 1996). The scaled Reynolds-shear stress, $\overline{uv}/U_m^2$, with U_m a suitable velocity scale, also decreases proportionally with b' as M_c increases. For the other Reynolds-stress components and other turbulence correlations or moments, no *a priori* description of the behaviour with M_c is currently available (Lele 2021). Individual Reynolds-stress components appear to scale differently, increasing Reynolds-stress anisotropy with M_c (Smits & Dussauge 2006). In this study, M_c scaling effects on the Reynolds stress, triple-velocity correlations and other turbulence correlations are considered to scale in a self-preserving manner, where it is revealed that these correlations scale with powers of b'. While self-preservation arguments have been made previously in the mixing layer (Pantano & Sarkar 2002; Smits & Dussauge 2006), the case of non-constant b' and M_c as the flow develops has yet to be considered. This work considers a compressible axisymmetric, or round, jet where M_c decays along the jet and b' is non-constant. This slowly evolving flow allows for the investigation of scaling and attenuation of turbulence moments, and provides novel insights on the effects of compressibility in shear flows.

Table 1 lists relevant studies of compressible mixing layers. The compressible mixing layer can be self-preserving in space or time, depending on its configuration, where after developing, the spreading rate, b', approaches a constant value less than its incompressible counterpart. Similar trends in the behaviour of the attenuation in the spreading rate have been observed in mixing layers of various configurations when plotted against M_c (Smits & Dussauge 2006). Here, M_c represents the propagation of disturbances in the frame of reference of the large-scale structures (Bogdanoff 1983). An empirical function, $\Phi(M_c)$, characterises these effects as the ratio between the compressible and incompressible spreading rates,

$$\Phi(M_c) = \frac{b'(M_c)}{b'_0}. \tag{1.1}$$

While M_c is the main parameter characterizing the attenuation, other parameters, such as the Reynolds number, geometry and initial upstream conditions, can also influence $\Phi(M_c)$. Feng & McGuirk (2016) suggest a modified behaviour in the axisymmetric mixing layers and found $\Phi(M_c)$ to express suppression at lower M_c compared with planar configurations. While this also tends to agree with an earlier experiment by Lau (1981), it is not supported in temporal mixing layers, as from Freund, Lele & Moin (2000). The lack of data for this behaviour and the unknown physical cause of this observation motivate further investigation. Here in the axisymmetric jet, the behaviour of $\Phi(M_c)$ has not yet been described, but is likely distinct from the mixing layer due to differences in flow structure and decaying M_c. The behaviour of $\Phi(M_c)$ in the axisymmetric jet is expected to resemble the axisymmetric, rather than planar, mixing layer configuration.

In addition to describing the behaviour of $\Phi(M_c)$, further challenges exist regarding scaling the Reynolds-normal stresses and where the trends do not show consensus. The scaling of $\overline{uv}/U_m^2$ with Mach number has been described in the mixing layer using self-preservation and scales proportional to $\Phi(M_c)$ (Vreman *et al.* 1996; Freund *et al.*

Authors	Marker	Method
Planar mixing layer		
Spatial		
Chinzei *et al.* (1986)	◊	Pitot
Papamoschou & Roshko (1988)	▽	Pitot
Samimy & Elliott (1990)	*	LDV
Goebel & Dutton (1991)	○	LDV
Debisschop *et al.* (1994)	+	LDV
Barre *et al.* (1994)	▷	Pitot
Clemens & Mungal (1995)	△	Pitot, PLMS, PLIF
Urban & Mungal (2001)	◁	PIV
Zhang *et al.* (2019)	♦	DNS
Temporal		
Vreman *et al.* (1996)	●	DNS
Pantano & Sarkar (2002)	▲	DNS
Matsuno & Lele (2020)	■	DNS
Axisymmetric mixing layer		
Spatial		
Lau *et al.* (1979)	×	LDV
Feng & McGuirk (2016)	□	LDV
Temporal		
Freund *et al.* (2000)	★	DNS
Axisymmetric jet		
Current study	-	PIV

Table 1. Comparison of previous studies of compressible shear layers.

2000; Pantano & Sarkar 2002; Smits & Dussauge 2006). As for the normalised Reynolds-normal stress, $\overline{u^2}/U_m^2$, experiments by Goebel & Dutton (1991) and Urban & Mungal (2001), and direct numerical simulation (DNS) by Freund *et al.* (2000) have shown relatively constant values with M_c, whereas studies from Samimy & Elliott (1990), Pantano & Sarkar (2002) and Matsuno & Lele (2020) found attenuation with increasing compressibility. These discrepancies lead to challenges in developing turbulence closure models which are able to physically represent these effects (Sarkar & Balakrishnan 1990; Wilcox 1992).

While compressible shear flows resemble their canonical incompressible analogues, which can be self-preserving, compressibility significantly affects the structure of turbulence. These differences include reduced pressure-fluctuation levels (Vreman *et al.* 1996), a reduction in transverse turbulence length scales (Freund *et al.* 2000) and inhibited pressure–strain momentum transfer (Pantano & Sarkar 2002). In these studies, the primary cause of the decreased turbulence levels is attributed to the reduction of the pressure–strain correlations which inhibits the redistribution of energy. This modified energy transfer motivates analysis of effects of compressibility on turbulence energetics through the Reynolds-stress-transport (RST) budgets. Furthermore, few experimental studies have been performed providing real-world validation of these theories, which are heavily reliant on observations made from DNS and are limited to lower Reynolds numbers.

Table 1 summarises the numerical and experimental techniques employed in compressible shear layers. Experimental methods for compressible shear flows are challenging due to the high-speed nature of the flow and sensitivity of the flow to external probes. While pitot tube measurements have been performed, they intrude on the flow and

introduce shockwaves; thus, laser diagnostics are the method of choice. Laser Doppler velocimetry (LDV) offers high sampling rates, but is limited to single-point measurements, making capturing spatial flow gradients with adequate resolution impractical. With the advent of short inter-frame cameras and dual-pulsed lasers, particle image velocimetry (PIV) is now widely used for compressible flows (Scarano 2008) and has been employed previously in the mixing layer by Urban & Mungal (2001). The current study employs PIV to provide detailed measurements of velocity-derived quantities at all locations, allowing the mean velocity profile, the half-width, b, and Reynolds stresses and their spatial derivatives to be measured at various M_c as the jet decays.

A perfectly expanded axisymmetric free jet is studied in the current work. This configuration, which has been historically overlooked in the literature, provides further insight into the compressible scaling of turbulence. The incompressible axisymmetric jet has been extensively studied (Wygnanski & Fiedler 1969; George 1989; Hussein, Capp & George 1994; George 1995), providing insight into the scaling of higher turbulence moments from self-preservation theory. In the compressible jet, many aspects of the flow have been studied, including the shock structure and mixing noise (Tam 1995; Wernet 2016). Regarding the turbulent mixing, early studies have attributed the reduction in the spreading rate in supersonic jets to density ratio effects (Kleinstein 1964) and little has been studied regarding the impact of the local Mach number on turbulence mixing or self-preservation considerations. The mixing layer, where a direct relationship between M_c and b' has been identified, is now a source of ambiguity in the jet where M_c decays when the jet expands and b' is no longer constant. Expanding on the self-preservation theory from George (1989), where b' is a main scaling parameter, turbulence scalings due to compressibility can be described using a self-preserving framework. The explicit connection between the convective Mach number, M_c, and the spreading rate, b', established in (1.1), allows for the attenuation of each turbulence moment to be described as a function of $\Phi(M_c)$.

This paper aims to establish and validate the turbulence scalings obtained from self-preservation for compressible shear flows. The governing equations and self-preservation analysis are introduced in § 2. Section 3 details the high-speed PIV experimental set-up used. In § 4, the mean velocity fields are analysed to characterise the compressibility effects on the jets spreading rate, defining the attenuation function, $\Phi(M_c)$, for the axisymmetric jet. In § 5, the scaling requirements are derived under the constraints of self-preservation, extending the analysis to include triple-velocity correlations through the RST equations. These scalings, which contain different powers of the spreading rate b', and consequently $\Phi(M_c)$, are then applied, collapsing the jet PIV data. Further insight is provided by investigating the jet turbulence energetics. Section 6 estimates the Reynolds-stress budgets, applying self-preservation scaling to examine the effects of compressibility and isolating the behaviour of the pressure strain. Finally, § 7 summarises the key findings and conclusions.

2. Background preliminaries

In compressible turbulence, fluctuating thermodynamic quantities need to be considered. Under certain conditions, these moments can be considered to have higher-order effects, thus simplifying the self-preservation analysis. This section reviews the governing equations in their self-preserving form for the compressible axisymmetric jet.

2.1. *Governing equations for the axisymmetric compressible jet*

Numerical studies typically solve the Navier–Stokes equations in conservative form and naturally employ mass-weighted, or Favre, averaging, where density moments are

absorbed in the averaging procedure. When using velocimetry data from experiments, the conventional Reynolds-averaged forms of these equations are more suitable for comparison, but result in several additional terms containing correlations of the fluctuating density. For sufficiently low Mach numbers, these additional correlations can be neglected. Morkovin (1964) suggests that for flows where the total temperature fluctuations are negligible, the magnitude of the density fluctuations can be approximated by the strong Reynolds analogy,

$$\frac{\sqrt{\overline{\rho''^2}}}{\rho} \approx -\frac{\sqrt{\overline{\Theta''}}}{\Theta} \approx (\gamma - 1)M^2 \frac{\sqrt{\overline{u^2}}}{U}, \tag{2.1}$$

with ρ the mean density, ρ'' the fluctuating density, Θ the mean temperature, Θ'' the fluctuating temperature, γ the specific heat ratio, u_i are the components (u, v, w) of the fluctuating velocities and U_i the components (U, V, W) of the mean velocities. This relation shows ρ''/ρ is largest in regions where high Mach number and turbulence intensity coincide. Originally derived for adiabatic flat-plate boundary layers, this has been extended to free shear flows such as mixing layers (Bradshaw 1977). For the current configuration where the stagnation temperature of the jet is approximately the ambient condition, the strong Reynolds analogy is valid, and since $\sqrt{\overline{u^2}}/U \approx 0.2$, $\sqrt{\overline{\rho''^2}}/\rho < 0.1$ for $M < 1.25$. Per the Cauchy–Schwarz inequality, for example, $\overline{uv} < \sqrt{\overline{u^2}}\sqrt{\overline{v^2}}$, terms such as $\overline{\rho'' uv}$ are an order-of-magnitude smaller than $\rho\overline{uv}$. This reduces the governing equations to

$$\boldsymbol{\nabla}_i\left(\rho U^i\right) = 0, \tag{2.2}$$

$$\rho U^j \boldsymbol{\nabla}_j U_i = \boldsymbol{\nabla}_i \overline{p} - \boldsymbol{\nabla}_j\left(\rho\overline{u_i u^j}\right) + \boldsymbol{\nabla}_j \overline{\tau}_i^j, \tag{2.3}$$

where i, j, k are indices reserved for spatial components, $\boldsymbol{\nabla}_k$ is the covariant derivative, $\overline{p}$ the mean pressure, $\overline{\tau}_i^j$ the mean stress tensor and overline indicating a temporal mean. In this section, superscripts indicate upper indices and not exponentiation, and repeated indices imply the Einstein summation convention. In addition, to determine the scaling of high-order moments, the scaling behaviour of the RST equations is necessary. To analyse the first-order scaling effects of the RST equations, only the significant terms are considered. As the pressure–strain correlation cannot be distinguished from the pressure-gradient term using only velocimetry measurements, it is assumed that

$$\overline{p''\boldsymbol{\nabla}_j u_i} + \overline{p''\boldsymbol{\nabla}_i u_j} \gg \boldsymbol{\nabla}_k\left[\overline{u_i p''}\delta_j^k - \overline{u_j p''}\delta_i^k\right]. \tag{2.4}$$

Thus, the pressure–diffusion terms are neglected to isolate and characterise the Mach number scaling on the pressure–strain term, which, unlike the pressure–diffusion, has a significant role in the Mach number suppression of turbulence. Again, terms containing fluctuating-density correlations are neglected, under the assumptions of the strong Reynolds analogy, and viscous diffusion is neglected for high-Re shear flows. This results in the first-order RST equations,

$$\begin{aligned}\left[\boldsymbol{\nabla}_k\left(\rho U^k \overline{u_i u_j}\right)\right] = &-\boldsymbol{\nabla}_k\left[\rho\overline{u_i u_j u^k}\right] - \left[\left(\rho\overline{u_j u^k}\right)\boldsymbol{\nabla}_k U_i + \left(\rho\overline{u_i u^k}\right)\boldsymbol{\nabla}_k U_j\right] \\ &+ \left[\overline{p''\boldsymbol{\nabla}_j u_i} + \overline{p''\boldsymbol{\nabla}_i u_j}\right] - \left[\overline{\left(\tau_j^k\right)''\boldsymbol{\nabla}_k u_i} + \overline{\left(\tau_i^k\right)''\boldsymbol{\nabla}_k u_j}\right],\end{aligned} \tag{2.5}$$

with p'' the fluctuating pressure and $\left(\tau_i^k\right)''$ the fluctuating viscous stress tensor. This equation consists of the terms contributing significantly to the turbulence energetics. These

are to be analysed through self-preservation, through which the effect of M_c on the scaling of these terms can be determined. The exact forms, without approximation, of (2.2)–(2.5) are found in Appendix A. As in the incompressible case, the terms grouped in the square brackets correspond to the advection, diffusion, production, pressure–strain and viscous-dissipation terms, respectively.

2.2. *Self-preservation of the compressible axisymmetric jet*

Self-preserving flows provide insight into the dynamical processes; self-preservation implies a state of equilibrium of the turbulence energetics. A flow is considered self-preserving if, when scaled, can produce collapsing profiles. For the incompressible jet, the scales are the centreline velocity and jet width, where according to classical theory, the jet width spreading rate, b', is considered a universal constant which 'forgets' its initial conditions (Townsend 1980). George (1989) challenged these ideas and instead classifies flows as fully, partially and locally self-preserving. The classification of which moments that can collapse depends on the scale determined through the similarity analysis of the governing equations. Under this classification, the incompressible jet is considered fully self-preserving when the profiles of all individual moments can collapse with the appropriate scale. Furthermore, George (1989) argues that the scale depends on the individual b' of the jet, which is not universal, and can differ depending on initial conditions and Reynolds number. Partially self-preserving flows then refer to flows where at least the Reynolds-shear stress collapses according to the scale $U_m^2 b'$ for the jet (George 1989). Lastly, locally self-preserving refers to flows where profiles are observed when normalised with a scale not determined through the governing equations.

For a compressible flow to be considered self-preserving, the thermodynamic quantities and their moments must develop either consistently with the other terms or be negligible. In the compressible mixing layer, assuming a turbulent Prandtl number $Pr_t \approx 1$, a Reynolds analogy can be made such that the density and temperature scale with the velocity (Pantano & Sarkar 2002; Smits & Dussauge 2006). After similarity analysis of the momentum equation, the main condition for self-preservation becomes $\overline{uv}/U_m^2 \propto b'$, where U_m is the velocity difference of the mixing layer. In the compressible mixing layer, b' is constant as the shear layer develops, which depends on the configured M_c, and satisfies this condition (Vreman *et al.* 1996). This scaling indicates at least a partially self-preserving flow, with full self-preservation contingent on how higher moments scale.

As opposed to the mixing layer, where compressibility effects are constant and M_c, b' and ρ do not vary with streamwise location, these quantities now change as the jet develops. Following George (1989), the functional dependencies of the similarity variables $U_m(x)$, $\rho_m(x)$, $p_m(x)$ and $R_{ij}(x)$ are left to be determined. Defining in physical components,

$$\eta = r/b(x), \tag{2.6}$$

$$U = U_m(x) f(\eta), \tag{2.7}$$

$$\rho = \rho_m(x) g(\eta), \tag{2.8}$$

$$p = p_m(x) h(\eta), \tag{2.9}$$

$$\overline{u^i u^j} = R_{ij}(x) r_{ij}(\eta), \tag{2.10}$$

where η is the normalised radius, and $f(\eta)$, $g(\eta)$, $h(\eta)$ and $r_{ij}(\eta)$ are shape functions. The density profile, $g(\eta)$, can be considered a function of the velocity

using a Crocco–Busemann relation (Smits & Dussauge 2006). The momentum of the compressible jet is conserved, as in the incompressible jet. To the first order,

$$J_0 = 2\pi \int_0^\infty \rho U^2 r \, \mathrm{d}r, \tag{2.11}$$

where J_0 is a constant. Substituting (2.6)–(2.8) into (2.11), it can then be shown that

$$\frac{U_m'}{U_m} = -\frac{1}{2}\frac{\rho_m'}{\rho_m} - \frac{b'}{b}, \tag{2.12}$$

which provides a relationship between the density, velocity, jet thickness and their streamwise gradients. With (2.2), (2.12), the streamwise momentum equation,

$$\rho U \frac{\partial U}{\partial x} + \rho V \frac{\partial U}{\partial r} = \frac{\partial}{\partial x}\overline{p} - \frac{1}{r}\frac{\partial r \rho \overline{uv}}{\partial r} - \frac{\partial \rho \overline{u^2}}{\partial x}, \tag{2.13}$$

can be shown for the jet using similarity variables,

$$\begin{aligned}\frac{1}{2}\frac{\rho_m'}{\rho_m}\left(gff - \frac{\partial gf}{\partial \eta}\frac{1}{g\eta}\int_0^\eta gf\hat{\eta}\mathrm{d}\hat{\eta}\right) - \frac{b'}{b}\left(gff + \frac{\partial gf}{\partial \eta}\frac{1}{g\eta}\int_0^\eta gf\hat{\eta}\mathrm{d}\hat{\eta}\right)\\ = -\frac{p_m b'}{bU_m^2\rho_m}\frac{\partial h}{\partial \eta} + \frac{p_m'}{U_m^2\rho_m}h - \frac{R_{12}}{bU_m^2}\frac{1}{\eta}\frac{d(gr_{12}\eta)}{\mathrm{d}\eta} + \frac{R_{11}b'}{bU_m^2}\eta\frac{d(gr_{11})}{\mathrm{d}\eta} - \frac{(R_{11}\rho_m)'}{U_m^2\rho_m}gr_{11}.\end{aligned} \tag{2.14}$$

In this form, the mean density effects on the jet flow is contained in the first term on the left of (2.12) and do not scale in a manner proportionally with the other terms. Therefore, self-preservation can only be approximated if the density gradients can be neglected, such that,

$$\frac{U_m'}{U_m} \approx -\frac{b'}{b}, \tag{2.15}$$

and will be shown in § 4.2 to hold for the current jet. Using this simplification, the first-order, without the Reynolds-normal stresses, self-preservation equation is then

$$-ff - \frac{1}{\eta}\frac{\partial f}{\partial \eta}\int_0^\eta f\hat{\eta}\,\mathrm{d}\hat{\eta} = \frac{R_{12}}{U_m^2 b'}\frac{1}{\eta}\frac{\mathrm{d}(r_{12}\eta)}{\mathrm{d}\eta}, \tag{2.16}$$

such that the Reynolds-shear stress must satisfy the scaling,

$$b' \propto \frac{R_{12}}{U_m^2}, \tag{2.17}$$

where a linear relationship between b and x is not assumed or required, and shear stress $\overline{uv}/U_m^2$ scales with the spreading rate b', and is consistent with that observed for the self-preserving compressible mixing layer (Vreman *et al.* 1996; Menaa 2003). The remaining Reynolds-normal stress and pressure in (2.14) scale according to

$$Const. \propto \frac{p_m}{\rho_m U_m^2} \propto \frac{p_m' b}{\rho_m U_m^2 b'} \propto \frac{R_{11}}{U_m^2} \propto \frac{R_{11}' b}{U_m^2 b'}. \tag{2.18}$$

The forms of the equations and scales recover the findings for the incompressible round jet by George (1989), which introduced that satisfying the condition of (2.17) is sufficient for a partially self-preserving flow, that is, the streamwise momentum equation is satisfied to the first order. For fully self-preserving flows, the normal stresses and all

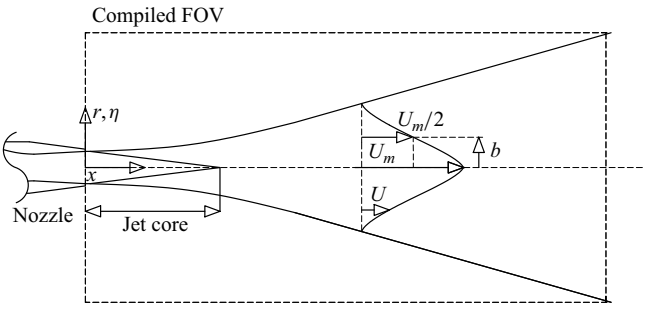

Figure 1. Schematic of jet flow.

Case	T_0 (K)	U_{jet} (m s^{-1})	P_0/P_{jet}	ρ_{jet}/ρ_0	Re_{jet}
$M_{jet} = 0.3$	293	102	1.09	0.95	36 000
$M_{jet} = 1.25$	293	375	2.70	0.51	86 000

Table 2. Jet parameters for different Mach numbers.

higher moments must behave according to the scales determined through self-preservation analysis. As the scaling and their requirements have yet to be established for compressible jets, it is unclear whether this condition can be met or its impact on describing the flow physics.

3. Experimental set-up

High-speed PIV is used to allow for detailed measurements of turbulence profiles and their streamwise developments. This section details the jet facility, as well as the PIV system used to measure the supersonic flow.

3.1. *Flow conditions*

Figure 1 is a schematic describing the free jet exhausting into ambient environment. A subsonic and supersonic case are investigated at Mach 0.3 and Mach 1.25, respectively. Building compressed air is supplied and controlled using an *Omega* PRG700 pressure regulator. The stagnation temperature, T_0, and stagnation pressure, P_0, are measured before flow enters a 0.5 m long stainless steel pipe of inner diameter 10.75 mm. The end of the pipe is fitted with a converging–diverging nozzle and is designed using the method of characteristics with an exit-to-throat area ratio of 1.047, with a nozzle exit diameter of 6.35 mm. Ambient laboratory conditions are also monitored, ensuring constant ambient conditions between tests. The stagnation-to-ambient nozzle pressure ratios are 1.87 and 2.70, corrected by 2 % and 5 %, respectively, to account for losses in the pipe assuming adiabatic Fanno flow for the Mach 0.3 and 1.25 cases. Both jets are considered fully turbulent, with $Re \approx 36\,000$ and 86 000 for the Mach 0.3 and Mach 1.25 cases, respectively. The turbulence intensity exiting the converging–diverging nozzle is estimated to be approximately 2.5 % at the jet centreline at $x/d = 1$ where measurements are available.

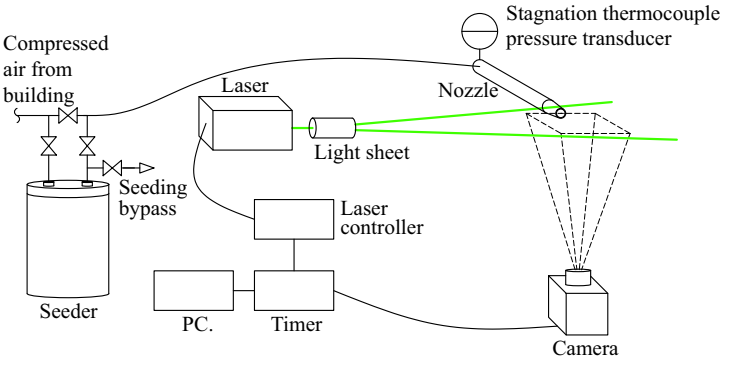

Figure 2. Schematic of free jet PIV experimental set-up.

3.2. *Particle image velocimetry system*

Figure 2 shows a diagram of the experimental set-up. Planar particle image velocimetry (PIV) was employed to measure two-component velocity fields in the plane bisecting the nozzle's centre plane. Velocity measurements were captured over a streamwise range from $x/d = 0$ to 25, using four overlapping fields-of-view (FOVs) of approximately 50 mm $\times$ 50 mm. The nozzle was mounted on rails, allowing it to slide independently of the laser and camera in the streamwise direction, ensuring consistent alignment between the light sheet and the camera across different measurements. The FOVs overlapped by 10.8 mm, covering approximately 25 % of the streamwise direction to ensure seamless data collection across the measurement region.

Both the jet and the ambient air were seeded with $\sim$1 μm di-ethyl-hexyl-sebacat (DEHS) particles, generated by a six-jet Laskin nozzle (*TSI* 9307-6). Although solid tracers are typically used for high-speed flows, DEHS was selected due to the need to seed the open environment of the jet flow. DEHS was preferred over solid particles due to the difficulties in collecting solid particles in an open environment while maintaining a suitable response time. Ragni *et al.* (2011) demonstrated that DEHS particles of this size have a response time of approximately 2 μs, which is comparable to solid tracers like TiO_2. This results in a Stokes number of $\approx$0.1, and ensures that the DEHS particles closely follow the flow's velocity fluctuations, providing accurate measurements of both mean velocity and turbulence quantities.

The PIV system consisted of a complementary metal–oxide–semiconductor (CMOS) camera (FastCAM Photron SA-5) with a 20 $\times$ 20 μm sensor and a resolution of 1024 $\times$ 1024 pixels camera was equipped with a Nikon AF Micro-Nikkor 60 mm f/2.8D lens and positioned 20 cm perpendicular to the light sheet. This results in a spatial pixel resolution of approximately 20 pixels mm^{-1}. The inter-frame time was set to 0.23 μs, independent of frame rate and resolution. A dual-cavity Nd:YLF laser (Photonics DM20-527-DM) was used as the illumination source, operating at a repetition rate of up to 10 kHz and delivering up to 20 mJ per pulse. The light sheet was formed using two spherical lenses and a cylindrical lens with a thickness of approximately 1 mm. At the nozzle exit – where the error due to the light-sheet thickness relative to the jet is greatest – the difference between the chord length at the laser-sheet edge intersecting the nozzle and the nozzle diameter is less than 1.25 %. Hence, the potential effect of an azimuthal orientation error can be considered negligible, and the measured velocity components approximate well the two-dimensional field along the PIV centre-plane. Measurements were conducted in dual-pulse mode, with a pulse separation interval of 1–1.5 μs, ensuring that particles moved

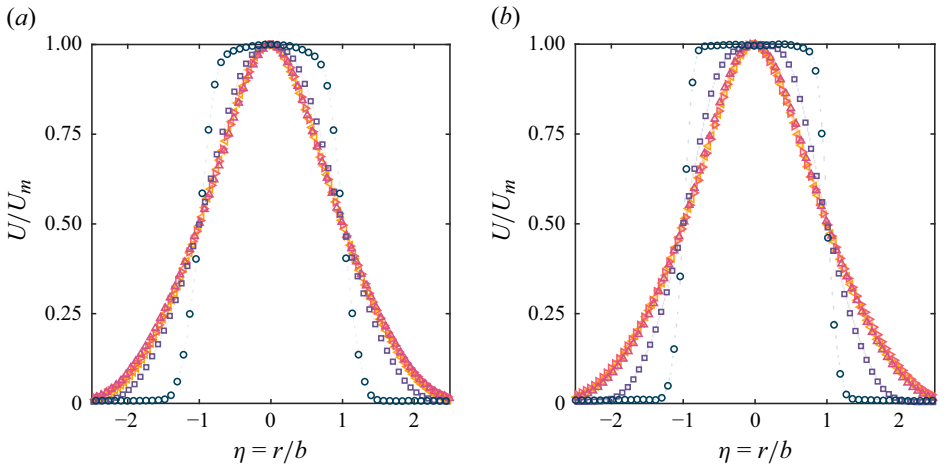

Figure 3. Development of velocity profiles. Every second point is shown for clarity. Axial positions: $x/d = 1.0$ (○); 3.0 (□); 7.0 (△); 10.0 (◁); 13.0 (▷). Shaded areas show 95 % expanded uncertainty bounds in respective colours. (*a*) Mach 0.3. (*b*) Mach 1.25.

approximately 7 pixels in the centre of the jet between image pairs. A silicon photodetector (Thorlabs DET02AFC) was used to verify the pulse separation timing to match the trigger signal.

The image pairs were processed using LaVision DaVis 10.2.0 software. Each test consisted of 2700 image pairs, with Reynolds stresses converging after approximately 750 pairs. The processing employed a multi-pass strategy, refining the vector field iteratively to improve accuracy, resulting in a 16 × 16 pixel interrogation window size with 75 % overlap. Sub-pixel accuracy when determining the particle image shift is achieved by peak fitting a Gaussian three-point estimator. This provides roughly 40 vectors across the jet's exit diameter. The 95 % expanded uncertainty bounds were calculated to account for random sampling errors (Benedict & Gould 1996) and are displayed where they exceed the marker size. Only random errors are displayed for the velocity moments as they are large in magnitude, hence more conservative than *a posteriori* uncertainty estimation methods available from the DaVis software, which does not consider the errors associated with the high-speed nature of the current flow.

4. Mean field characteristics

Figure 3 shows the mean velocity profiles, U/U_m, just outside the nozzle starting at $x/d = 1$. The half-width b, defined at the radial location where $U = (1/2)U_m$, is used as the length scale. Due to reflections of the light sheet off the nozzle, the jet-exit velocity profile and data are unavailable for $x/d \lessapprox 0.8$. The profiles show the jet-core region and are found to approach the Gaussian profile distribution, indicative of self-similarity as early as $x/D = 10$. This rapid development is likely due to the configuration of the current upstream nozzle condition. Although the current jet is expelled through a convergent–divergent nozzle, the influence of the boundary layer is expected to be significant in accelerating the development, as is the case for jets expelled from a pipe flow. Jets expelled from pipes have been shown to develop faster to self-preservation conditions than 'top-hat' jets (Nguyen & Oberlack 2024).

Figure 4 shows the collapse of the mean velocity profiles, U/U_m, in both incompressible and compressible cases. The vorticity thickness, which is defined as the location

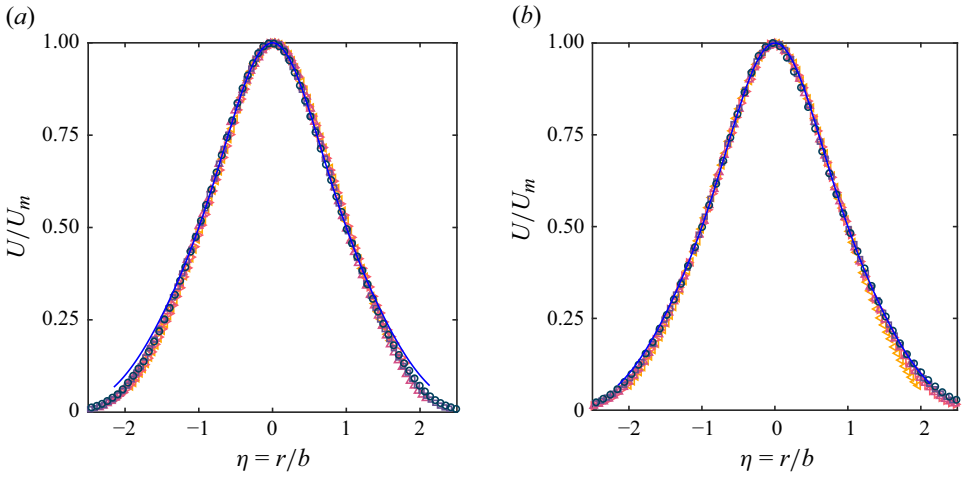

Figure 4. Self-preserving velocity profiles comparison between compressible and incompressible jets. LDV from Hussein *et al.* (1994) (——). Every fourth point is shown for clarity. (*a*) Mach 0.3. Axial positions: $x/d = 17.5$ (○) ; 20.0 (□); 22.5 (△); 25.0 (◁); 27.5 (▷); (*b*) Mach 1.25. Axial positions: $x/d = 12.5$ (○); 15.5 (□); 18.5 (△); 21.5 (◁); 24.5 (▷).

of maximum shear rate, is commonly used in mixing layer studies. For self-similar mean velocity profiles, the vorticity thickness is directly proportional to the half-width, $\delta_\omega = 1.4b$. Thus, the trends and qualitative scaling behaviour of the jet thickness are the same using either b or δ_ω as length scales. The mean profiles are shown after $x/d = 17.5$ and 12.5, for the Mach 0.3 and Mach 1.25 jets, respectively. These locations correspond to where the Reynolds-shear stress is self-preserving, which will be shown in the following sections. Despite the compressibility effects of the Mach 1.25 jet, the mean velocity profile does not significantly differ, which was observed in compressible mixing layers (Smits & Dussauge 2006). For reference, incompressible jet data collected using LDV from Hussein *et al.* (1994) are overlaid.

In incompressible jets, the profiles can be collapsed using the axial distance, x, through the classical self-similarity scaling $x \propto b$. Due to compressibility effects in the Mach 1.25 jet, b is no longer directly proportional to x, and scaling the velocity profiles with b is necessary. This scaling can be observed in figure 5(*a*), which plots the development of b of both the Mach 0.3 and Mach 1.25 jets. Near the exit of the nozzle, Mach number effects are significant and b develops with a varying slope not observed in the Mach 0.3 jet. Towards the end of the domain where the Mach 1.25 approaches a subsonic value, the slopes approach a similar value, corresponding to 0.085 and 0.088 for the Mach 0.3 and Mach 1.25 jets, respectively. Although these downstream spreading rates are not identical, the rates at the end of the domain fall within the range of 0.079–0.1, previously reported for incompressible axisymmetric jets (Gutmark 1983). The discrepancy in slope is attributed to sensitivity to initial conditions and parameters such as Reynolds number (George 1989). Likewise, figure 5(*b*) shows differing slopes for the inverse of the centreline velocity, where for Mach 0.3, the slope is approximately 0.016 compared with 0.014 for $M_{jet} = 1.25$. These observations are consistent with self-similarity behaviour, i.e. $U_m \propto x^{-1}$. Based on 95 % of the jet-exit velocity, the end of the jet potential core is 5.2 x/d and 6.3 x/d for the Mach 0.3 and Mach 1.25 jets, respectively. The extended length of the jet core in the Mach 1.25 is a result of the density ratio and the decreased mixing due to Mach number effects, which is further discussed in the following section.

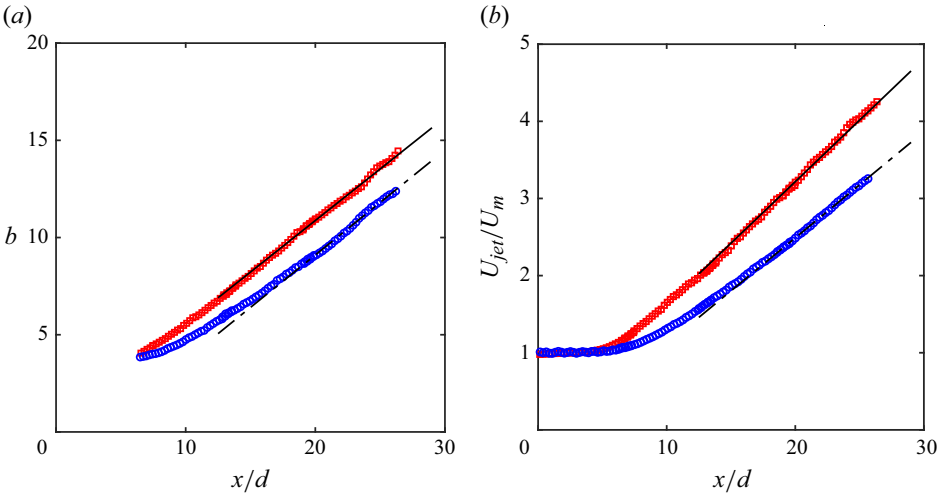

Figure 5. Approximate power laws. Mach 0.3 (□) and Mach 1.25 (○). (*a*) b development (*mm*). Overlaid lines with slope of 0.083 (——) and 0.085 (— · —) in *mm*/*mm*; (*b*) U_m development. Overlaid lines with slope of 0.016 (——) and 0.014 (— · —).

4.1. *Kleinstein–Witze scaling*

Methods approximating the centreline velocity development for compressible axisymmetric jets has been addressed through the Kleinstein–Witze scaling. Assuming an eddy viscosity in the form (Ferri, Libby & Zakkay 1964)

$$\rho \nu_t = (\kappa/4) b \rho_m U_m, \tag{4.1}$$

where κ is a proportionality constant, the solution of the linearised momentum equation describes the centreline velocity decay in the form,

$$\frac{U_m}{U_{jet}} = 1 - \exp\left[\frac{-1}{2\kappa\left(\frac{x}{d}\right)\left(\frac{\rho_{jet}}{\rho_0}\right)^{1/2} - X_c}\right], \tag{4.2}$$

where X_c is a constant describing the jet core length (Kleinstein 1964). Figure 6 shows the centreline velocity development with fitted functions of (4.2) overlaid. The constants are found to be $\kappa = 0.0796$ and $X_c = 0.487$ for $M_{jet} = 0.3$, and $\kappa = 0.0842$ and $X_c = 0.511$ for $M_{jet} = 1.25$. The scaling was originally proposed with constants $\kappa = 0.074$ and $X_c = 0.7$. Witze (1974) suggests κ to have some Mach number dependence. Studies by Lau, Morris & Fisher (1979), Lau (1981) and Wernet (2016) confirm that (4.2) generally captures the effect of density, but large scatter remains in the values reported from different studies for κ and X_c. Here, the lower values of X_c reflect the pipe-nozzle configuration on the jet initial condition.

Kleinstein (1964) also shows that the total enthalpy, H, is given in the form,

$$\frac{H - H_0}{H_{jet} - H_0} = 1 - \exp\left[\frac{-1}{2\kappa Pr_t^{-1}\left(\frac{x}{d}\right)\left(\frac{\rho_{jet}}{\rho_0}\right)^{1/2} - X_c}\right], \tag{4.3}$$

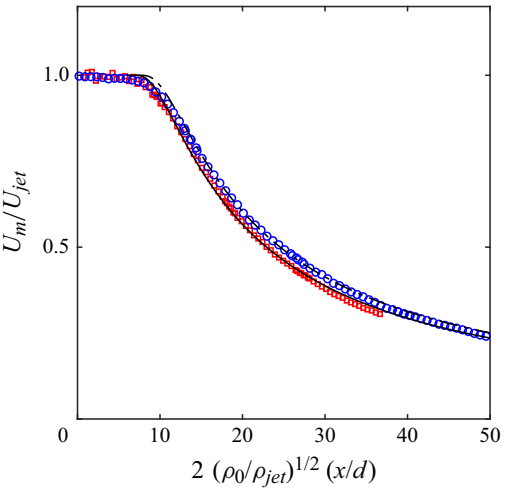

Figure 6. Downstream development of U_m/U_{jet} for Mach 0.3 (□) and Mach 1.25 (○). Witze–Kleinstein functions for Mach 0.3 (——) and Mach 1.25 (— · —).

where $Pr_t = 0.715$ was experimentally determined by Kleinstein (1964). This relation allows the centreline total enthalpy to be determined from the fit constants of the velocity data. This allows further derived properties like the density, temperature and Mach number to be estimated on the jet centreline, which are used in the following section to aid in the scaling of the jet.

4.2. *Compressibility and spreading rate*

Compressibility impacts b' through two key mechanisms: the mean density ratio and the convective Mach number, M_c. Where the mean density gradient affects b' through continuity, M_c affects turbulence mixing through the attenuation of the Reynolds stresses. These two effects have been shown to act independently (Bradbury & Riley 1967; Barre, Quine & Dussauge 1994). Brown & Roshko (1974) compared subsonic mixing layers of different density ratios with supersonic mixing layers having the same density ratios. The behaviour of supersonic mixing layers could not be described by density variations alone, unlike the behaviour observed in compressible boundary layers. Although density variations influence the spreading rate, this effect is generally only significant at density ratios >7 in both subsonic (Brown & Roshko 1974) and supersonic mixing layers (Menaa 2003). Therefore, at moderate density ratios, b' is mainly a function of M_c in supersonic mixing layers. Figure 7 shows the spreading rate, b', for $M_{jet} = 0.3$ and $M_{jet} = 1.25$. To reduce noise in the slope, a low-order polynomial fit of the half-width data is used to calculate the rate.

The downstream development of M_c is shown in figure 8, where the shaded area shows the 95 % expanded uncertainty bounds. For an identical specific heat ratio of the gases on both sides of the shear layer, the convective velocity is defined as

$$U_c = \frac{a_l U_m + a_m U_l}{a_m + a_l}, \tag{4.4}$$

where a is the speed of sound, and the high-speed and low-speed sides are noted with subscripts m and l, respectively (Papamoschou & Roshko 1988). In the free jet, the centreline quantity corresponds to the high-speed side and the low-speed side ambient

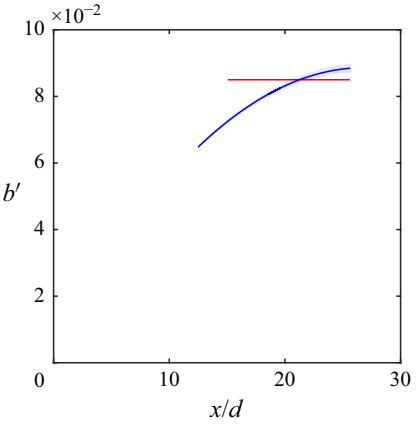

Figure 7. Downstream development of b' in mm/mm from curve fits of b for Mach 0.3 (——) and Mach 1.25 (——). Shaded areas show 95 % expanded uncertainty bounds in respective colours.

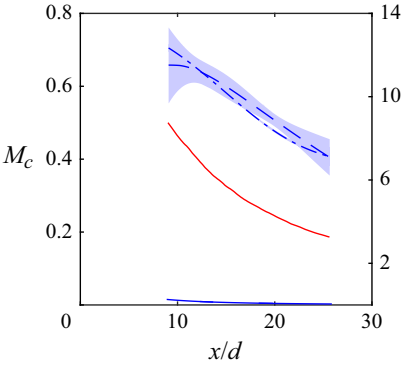

Figure 8. Downstream development of M_c (——) left axis, b'/b (- - -), U'_m/U_m (— · —) and $(1/2)\rho'/\rho$ (——) right axis for Mach 1.25. Shaded areas show 95 % expanded uncertainty bounds in respective colours.

conditions where $U_l = 0$, where M_c simplifies to the following relation,

$$M_c = \frac{U_m}{a_m + a_l}. \tag{4.5}$$

Here, a_m is approximated using the temperature determined from the total enthalpy from (4.3) and a_l from the ambient static temperature.

Figure 8 depicts the downstream development of the streamwise gradients of U_m and b as ratios U'_m/U_m and $-b'/b$. In the region $x/d > \approx 10$, U'_m/U_m and $-b'/b$ differ less than the experimental uncertainty, thus justifying the approximation of (2.15) and implies ρ'_m/ρ is generally small. Satisfying (2.15) implies neglecting the first term of (2.14). This approximation extends previous observations in mixing layers (Brown & Roshko 1974; Menaa 2003) to jets, showing that at the current density ratios, the reduction in b' can be attributed primarily to M_c effects.

To compare the effect of compressibility on the spreading rate between the jet and the mixing layer, $\Phi(M_c)$ defined in (1.1) is employed. Here, the spreading rate of the $M_{jet} = 1.25$ jet as it decays is normalised by the value from the incompressible $M_{jet} = 0.3$ jet from figure 7. Unlike the mixing layer, $\Phi(M_c)$ in the jet changes as M_c decays. Figure 9

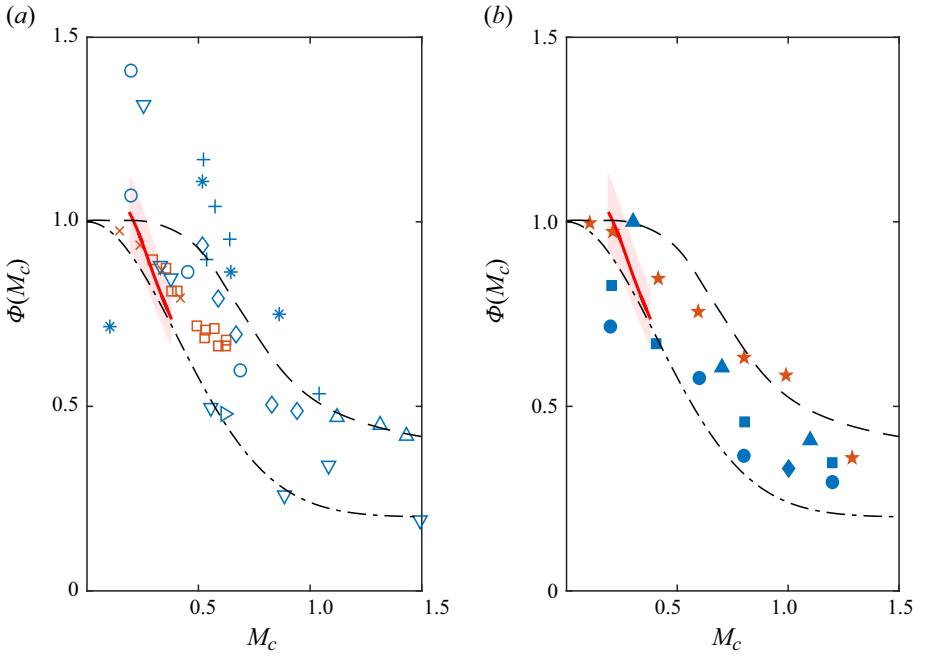

Figure 9. Shear layer thickness growth rate suppression. Current study in (——) compared with (*a*) previous experimental studies and (*b*) numerical studies. For the legend of used markers, see table 1. Axisymmetric data coloured in red and planar data in blue. Curve from Dimotakis (1991) (— · —) and Langley experimental curve from Kline, Cantwell & Lilley (1982) (- - -). Shaded areas show 95 % expanded uncertainty bounds.

compares the behaviour of $\Phi(M_c)$ in the current jet data with earlier results for mixing layers. Similar trends between the data suggest that the local M_c strongly influences $\Phi(M_c)$. Although the magnitude of the values observed in the present jet is similar to those of the planar measurements from Papamoschou & Roshko (1988), the slope of the jet data tends to be more similar to the annular mixing layer than the planar mixing layer experiments. Feng & McGuirk (2016) suggests the hypothesis where axisymmetric symmetry modifies the behaviour of $\Phi(M_c)$, observing that the spreading rate suppression occurs at lower M_c, where the cause of this phenomenon remains unelucidated. It thus appears that while $\Phi(M_c)$ is mainly a function of M_c, geometric effects also have an influence.

5. Self-preservation scaling of velocity correlations

As established in § 2.2, self-preservation requires $\overline{uv}/U_m^2$ to scale proportionally with the spreading rate, where the compressibility effects are characterised by $\Phi(M_c)$. Although confirmed for the mixing layer, this section verifies the scaling for the axisymmetric compressible jet. The self-preservation arguments for the remaining Reynolds stresses and triple-velocity correlations are made showing their scaling with compressibility effects.

5.1. *Reynolds-shear stress scaling*

Figure 10(*a*) presents the Reynolds-shear stress profiles for the Mach 0.3 jet, normalised using the classical scaling U_m^2. For comparison, the incompressible LDV data from Hussein *et al.* (1994) is overlaid. From axial positions beyond $x/d = 17.5$, a good collapse of the profiles is observed and agrees with the LDV measurement from Hussein *et al.*

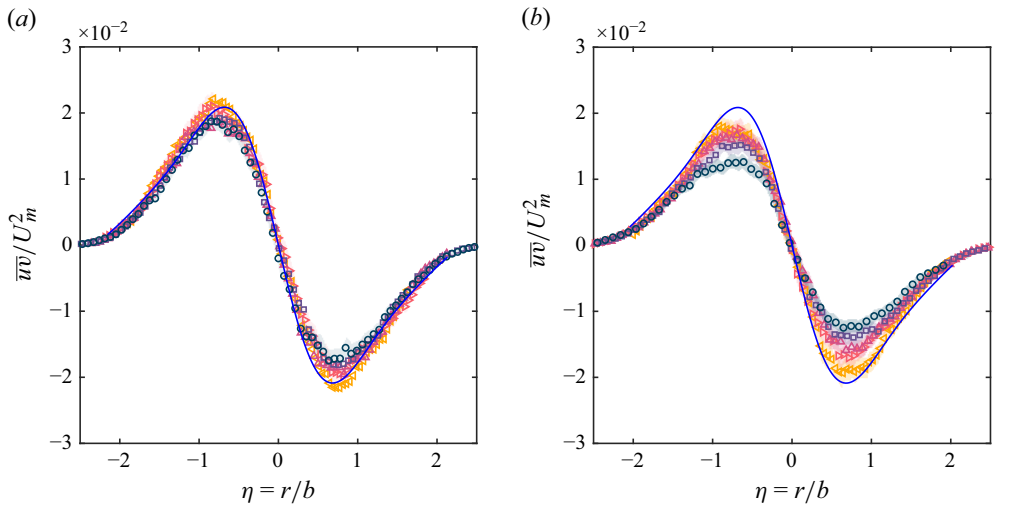

Figure 10. Reynolds-shear stress. Classical scaling with U_m^2. LDV data from Hussein *et al.* (1994) (——). Every fourth point shown for clarity. Shaded areas show 95 % expanded uncertainty bounds in respective colours. (*a*) Mach 0.3. Axial positions: $x/d = 17.5$ (○) ; 20.0 (□); 22.5 (△); 25.0 (◁); 27.5 (▷); (*b*) Mach 1.25. Axial positions: $x/d = 12.5$ (○); 15.5 (□); 18.5 (△); 21.5 (◁); 24.5 (▷).

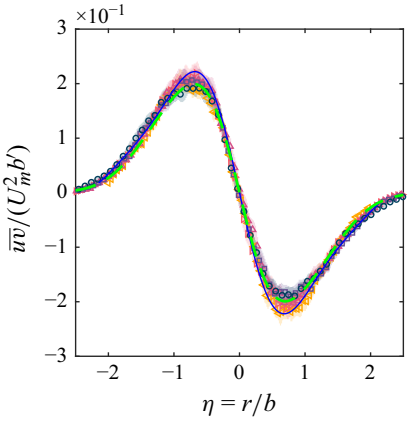

Figure 11. Mach 1.25. Collapse of $\overline{uv}$ profiles with scaling $U_m^2 b'$. Same legend as figure 10(*b*). Profile calculated from (5.1) (- - -).

(1994). The similarity of the Reynolds stresses, like the mean profiles discussed in § 4, are observed to occur earlier upstream due to the initial conditions of the current jet. In contrast, for $M_{jet} = 1.25$ in figure 10(*b*), the collapse of the Reynolds-stress profiles is less satisfactory and the amplitude is lower in the upstream regions where M_c is larger.

In figure 11, the profiles of Reynolds stress using the self-preservation scaling, $U_m^2 b'$, collapse better, especially for the data upstream where M_c is elevated. Using this scaling, the Reynolds-shear stress in the Mach 1.25 jet exhibits similarity at approximately $x/d = 12.5$. This scaling also collapses the incompressible data. The scaled Reynolds-shear stress profile can be calculated using the mean velocity when rearranging and integrating (2.16) in the following manner:

$$\frac{R_{12} r_{12}}{U_m^2 b'} = \frac{1}{\eta} \int_0^{\eta} \left(-\tilde{\eta} f f - \frac{\partial f}{\partial \tilde{\eta}} \int_0^{\tilde{\eta}} f \hat{\eta} \, \mathrm{d}\hat{\eta} \right) \mathrm{d}\tilde{\eta}. \tag{5.1}$$

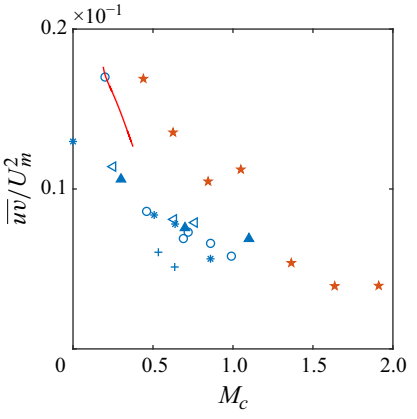

Figure 12. Maximum Reynolds stress $\overline{uv}$ normalised by U_m^2 as a function of M_c for mixing layers and the present jet data. Samimy & Elliott (1990) (∗), Goebel & Dutton (1991) (○), Urban & Mungal (2001) (◁), Debisschop, Chambers & Bonnet (1994) (+), Pantano & Sarkar (2002) (▲), Freund *et al.* (2000) (★), current study (-).

The Reynolds-shear stress profile calculated from (5.1) is plotted and aligns with the data, validating the scaling and tacitly supporting the underlying assumptions underpinning (2.1) and (2.15). Figure 12 compares the behaviour of the max Reynolds-shear stress, $\overline{uv}/U_m^2$, as a function of M_c, providing a comparison to mixing layer data. Again, a decreasing trend in amplitude with M_c is observed. Collapse of the Reynolds-shear stress indicates a form of self-preservation is observed in the compressible jet and suggests the flow is at least partially self-preserving. Self-preservation of other turbulence moments is unclear and is now investigated.

5.2. *Reynolds-normal stress scaling*

The proposed scaling of the streamwise Reynolds stress, $\overline{u^2}$, derived from the self-preservation analysis of (2.14), is $R_{11} \propto U_m^2$. This scaling suggests that assuming self-preservation implies that b' and, therefore, compressibility do not affect this Reynolds-stress component. Figure 13(*a*) plots $\overline{u^2}/U_m^2$ for $M_{jet} = 1.25$, where profiles do not collapse. Instead, the peak values of $\overline{u^2}/U_m^2$ increases progressively as the jet evolves downstream, a trend also seen in the Reynolds-shear-stress profiles of $\overline{uv}/U_m^2$. With this observation, figure 13(*b*) now shows the scaling $\overline{u^2}$ normalised by $b'U_m^2$, which collapses the profiles at $x/d > 15$. Although this scaling does not have any physical basis from a self-preservation standpoint, it produces a more consistent collapse of the data across the downstream locations. This scaling suggests that factors other than those predicted by self-preservation theory influence the compressible behaviour of $\overline{u^2}$.

In figure 14(*a*), the maximum magnitudes, $\overline{u^2}/U_m^2$, at different streamwise locations, are compared at different M_c for the jet and mixing layer. Two distinct trends emerge from the literature. Goebel & Dutton (1991) and Freund *et al.* (2000) (at $M_c > 0.4$) observed scaling independent with M_c, consistent with the similarity assumption. However, Elliott & Samimy (1990), Samimy & Elliott (1990) and Matsuno & Lele (2020) report a suppression of $\overline{u^2}/U_m^2$ as M_c increases. The current jet data trend aligns with the latter set of studies. While some scatter and asymmetry are observed in the profiles, the measurements remain within the 95 % uncertainty bounds shown in the shaded colours. Figure 14(*b*)

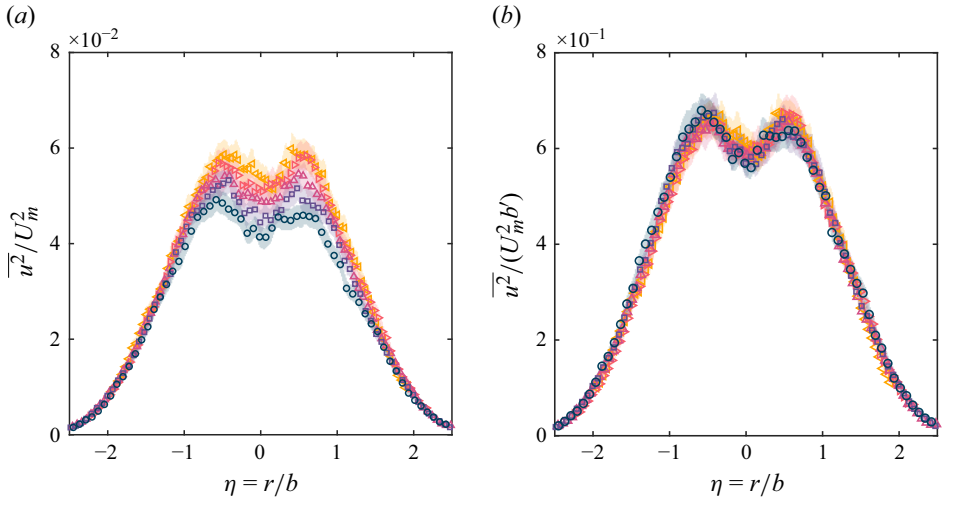

Figure 13. Reynolds-normal stress $\overline{u^2}$. Axial positions: $x/d = 15.0$ (○); 17.5 (□); 20.0 (△); 22.5 (◁); 25.0 (▷). Shaded areas show 95 % expanded uncertainty bounds in respective colours. (*a*) Mach 1.25. Classical scaling with U_m^2; (*b*) Mach 1.25. Collapse of $\overline{u^2}$ profiles with scaling $U_m^2 b'$.

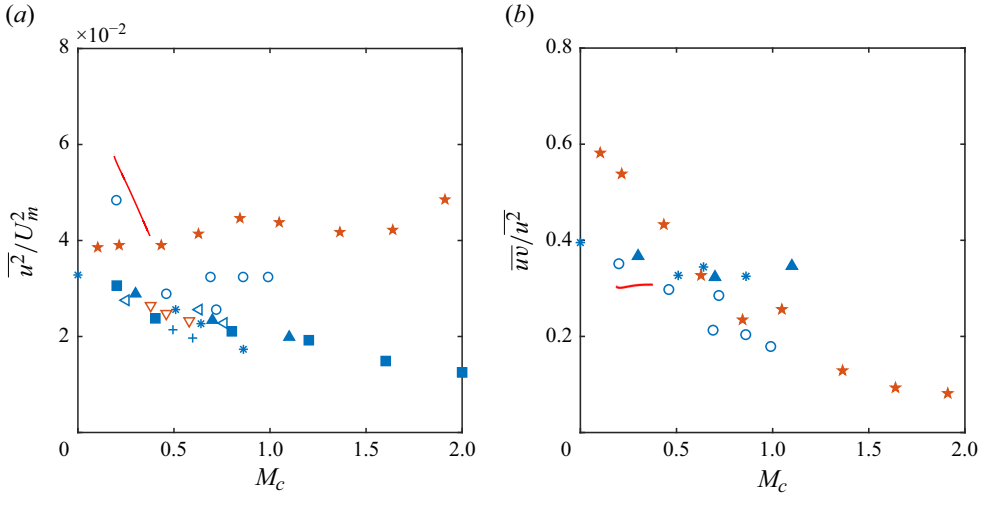

Figure 14. Maximum Reynolds stresses as a function of M_c for mixing layers and present jet data. Samimy & Elliott (1990) (∗), Goebel & Dutton (1991) (○), Debisschop *et al.* (1994) (+), Urban & Mungal (2001) (◁), Pantano & Sarkar (2002) (▲), Matsuno & Lele (2020) (■), Feng & McGuirk (2016) (□), Freund *et al.* (2000) (★), current study (-). (*a*) Maximum Reynolds stress $\overline{u^2}$ normalised by U_m^2. (*b*) Ratio of the maximum Reynolds stresses $\overline{uv}/\overline{u^2}$.

examines the ratio of $\overline{uv}$ to $\overline{u^2}$ as a function of M_c. This ratio remains nearly constant at approximately 0.6, consistent with findings in mixing layer studies reporting $\overline{u^2}/U_m^2$ suppression (Samimy & Elliott 1990; Pantano & Sarkar 2002), and supports the evidence that $\overline{uv}$ and $\overline{u^2}$ are attenuated by compressibility proportionally.

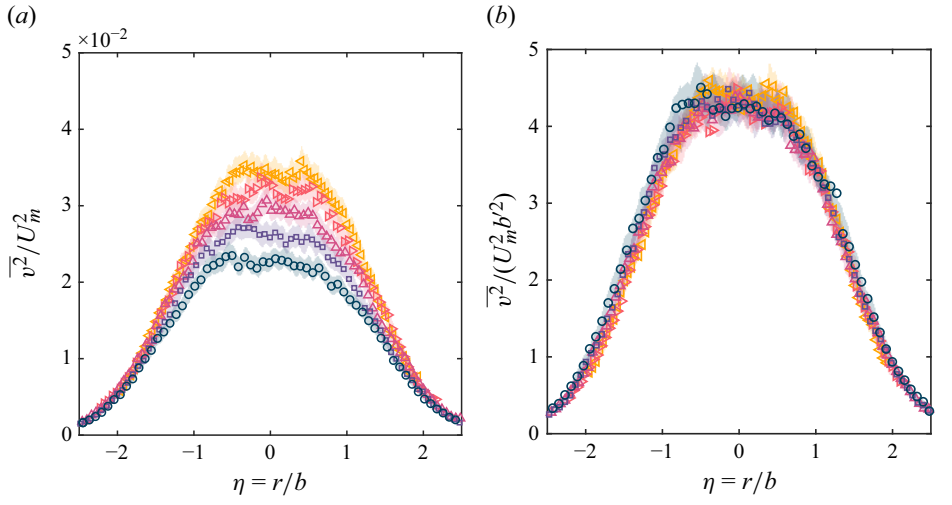

Figure 15. Comparison of classical and self-preservation scaling of $\overline{v^2}$. Mach 1.25 jet. Axial positions: $x/d = 15.0$ (○); 17.5 (□); 20.0 (△); 22.5 (◁); 25.0 (▷). Shaded areas show 95 % expanded uncertainty bounds in respective colours. (*a*) Classical scaling with U_m^2; (*b*) Collapse of $\overline{v^2}$ profiles with self-preservation scaling $U_m^2 b'^2$.

For $\overline{v^2}$, substituting (2.6)–(2.10) yields the radial-momentum equation,

$$\rho U \frac{\partial V}{\partial x} + \rho V \frac{\partial V}{\partial r} = \frac{\partial \overline{p}}{\partial r} + \frac{1}{r}\frac{\partial}{\partial r}\left(r\rho\overline{v^2}\right), \tag{5.2}$$

and performing the similarity analysis results in the following normalised scalings:

$$Const. \propto \frac{p_m}{\rho_m U_m^2 b'^2} \propto \frac{R_{22}}{U_m^2 b'^2}, \tag{5.3}$$

or $\overline{v^2} \propto U_m^2 b'^2$. From figure 15(*a*), profiles of $\overline{v^2}/U_m^2$ shows strong attenuation with M_c. Instead, figure 15(*b*) plots the profiles using the self-preservation scaling from (5.3). Now, the profiles of $\overline{v^2}$ collapse. Figure 16 compares the behaviour of the maximum of $\overline{v^2}$ with M_c with the mixing layer literature. Unlike, $\overline{u^2}$, the behaviour of $\overline{v^2}$ shows a consensus with the literature where attenuation with M_c is observed.

To further investigate the scaling observed in the Reynolds-normal stresses, the pressure term is now considered. Pressure can be estimated by integrating the radial momentum equation from $\overline{p}_\infty$, where there is no turbulence to any location, r. This yields $\overline{p}_\infty - \overline{p} = \rho\overline{v^2}$ which is substituted into the streamwise momentum equation, resulting in

$$\rho U \frac{\partial U}{\partial x} + \rho V \frac{\partial U}{\partial r} = \frac{1}{r}\frac{\partial r\rho\overline{uv}}{\partial r} - \frac{\partial}{\partial x}\left(\rho\overline{u^2} - \rho\overline{v^2}\right). \tag{5.4}$$

To investigate the scaling of this term, the similarity substitution $\overline{u^2} - \overline{v^2} = \Psi(x)\psi(\eta)$ is made, yielding

$$Const. \propto \frac{R_{12}}{U_m^2 b'} \propto \frac{\Psi}{U_m^2} \propto \frac{\Psi' b}{U_m^2 b'}. \tag{5.5}$$

Figure 17 plots the normal stress difference, showing profiles collapse under this scaling for the compressible jet flow. The same profile is also observed for $M_{jet} = 0.3$.

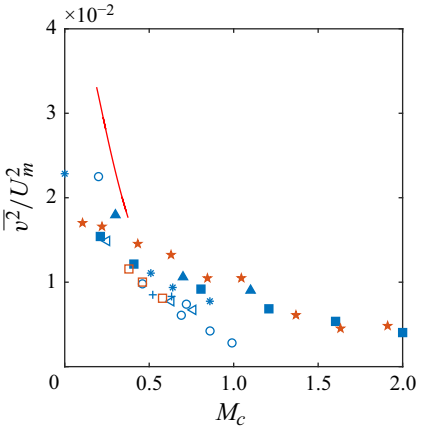

Figure 16. Maximum Reynolds stress $\overline{v^2}$ normalised by U_m^2. Same legend as figure 14.

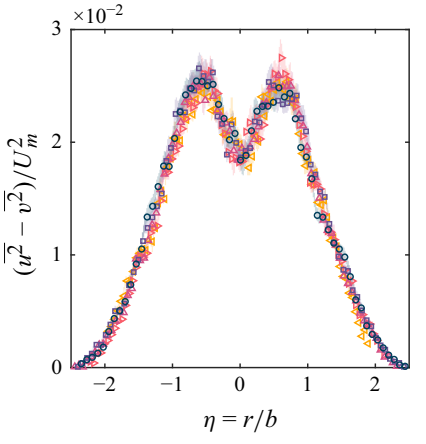

Figure 17. Collapse of profiles of Reynolds-normal stress difference for the Mach 1.25 jet. Marker axial positions have the same legend as figure 15.

For the $M_{jet} = 1.25$ case, this observation is unexpected since $\overline{u^2}$, unlike $\overline{v^2}$, did not obey self-preservation scaling previously. Upon closer examination, the pressure in the streamwise (2.14) and radial (5.2) momentum equations suggests different scaling. In the streamwise equation, $p_m \propto \rho_m U_m^2$, whereas in the radial equation, $p_m \propto \rho_m U_m^2 b'^2$. The pressure term may involve two parts and complex dynamical interactions emphasised by compressibility. Self-preservation can be satisfied when considering the aggregate of the Reynolds-normal stresses.

Figure 18 shows the streamwise development of the local-maximum scaled-Reynolds stresses for the Mach 1.25 jet. It shows that when using the correct scale determined using self-preservation arguments, the Reynolds stresses can be considered self-preserving under Mach number effects. The scaled Reynolds-shear stress, $\overline{uv}/U_m^2 b'$, is the first to plateau, at approximately $x/d = 12.5$, whereas the normal stresses appear to plateau further downstream, at approximately $x/d = 15$. The relatively early state of preservation is due to the upstream condition of the jet as discussed previously. To further investigate these scaling concepts, self-preservation analysis of the Reynolds-stress-transport equations are required for higher-order turbulence moments.

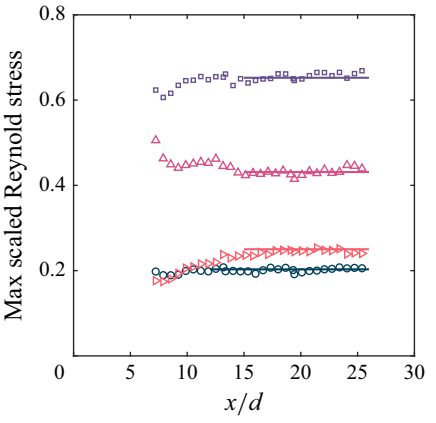

Figure 18. Development of maximum scaled Reynolds stress for Mach 1.25 jet: $\overline{uv}/U_m^2 b'$ (○); $\overline{u^2}/U_m^2 b'$ (□); $\overline{v^2}/U_m^2 b'^2 \cdot 0.1$ (△); $(\overline{u^2} - \overline{v^2})/U_m^2 \cdot 10$ (◁). Solid lines in respective colours represent the range where Reynolds stresses are considered self-preserving.

5.3. *Reynolds-shear stress-anisotropy parameter*

The anisotropy tensor, $\beta_{ij} = \overline{u_i u_j}/\overline{u_k u_k}$, is commonly used to describe the effects of compressibility on the anisotropy of the Reynolds stresses. From the self-preservation analysis, β_{ij} can be directly related to compressibility effects through $\Phi(M_c)$. The Reynolds-shear stress-anisotropy parameter, β_{12}, can be written as

$$\beta_{12} = \frac{\overline{uv}}{\overline{u^2} + \overline{v^2} + \overline{w^2}}. \tag{5.6}$$

Using the self-preservation scalings, $\overline{uv} \propto U_m^2 b'$, $\overline{v^2} \propto U_m^2 b'^2$ and $\overline{w^2} \propto U_m^2 b'^2$, and the experimentally observed scaling $\overline{u^2} \propto U_m^2 b'$, then substituting the relations and with the relation $b' \propto \Phi(M_c)$, with some manipulation, the parameter β_{12} can be written as

$$\beta_{12} = \frac{1}{C_1 + C_2 \Phi(M_c)}, \tag{5.7}$$

where C_1 and C_2 are constants. Figure 19 plots β_{12} at $\eta = 1$, corresponding to the point of maximum shear. Here, $\overline{w^2}$ is approximated with $\overline{v^2}$, which from symmetry is expected to scale similarly. The solid line represents (5.7) fitted to the data, with constants $C_1 = 4.4$ and $C_2 = 1.8$, showing the suitability of the function to characterise β_{12}. In the current jet, the parameter β_{12} increases with M_c. Like the Reynolds stresses, various behaviours of β_{12} have been reported, also plotted are data from Freund *et al.* (2000), showing a decrease with M_c, and Pantano & Sarkar (2002), where a more constant behaviour is observed. Again, challenges are observed for turbulence models in compressible flows as there is no consensus on fundamental scaling parameters.

5.4. *Optimal spreading rate scaling*

The spreading rate, b', plays a critical role in scaling turbulence moments. A root-mean-square-deviation (RMSD) minimisation method was developed to identify the optimal power of b' for each profile within the range of self-preservation. The RMSD minimisation method provides an objective measure of profile collapse, offering a quantitative approach to compare the degree of alignment across profiles. First, to ensure comparable errors across normalised profiles, the Reynolds stresses and triple-velocity correlations were

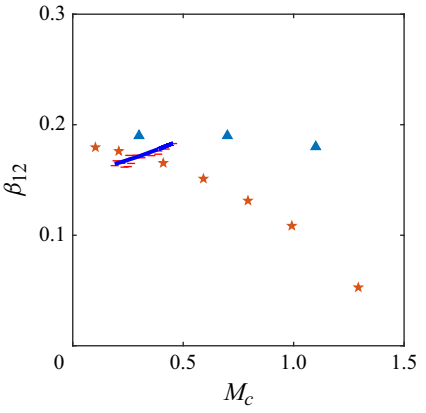

Figure 19. β_{12} scaling. Mach 1.25 jet (–) and fitted function (——) from (5.7). Freund *et al.* (2000) (★); Pantano & Sarkar (2002) (▲).

scaled and normalised to a peak magnitude of unity using the scalings $U_m^2 b'^n$ for the Reynolds stresses and $U_m^3 b'^n$ for the triple-velocity correlations. Normalising to a peak magnitude of unity ensures that the relative error remains consistent across different profiles, enabling more accurate comparisons. Since the data points are not on a fixed grid after radial normalisation, the η axis is divided into discrete bins. The RMSD is computed for each bin and the total RMSD for the profile is obtained by summing the individual bin RMSDs in quadrature. A study was performed to ensure that the choice of bin size did not affect the final RMSD value. Figure 20 shows that the minima of the RSMD curves are close to the integer values reported for the scalings of b'.

5.5. *Self-preservation of the Reynolds-stress-transport equations*

The RST equations describe the production, transport and dissipation of each Reynolds stress. In the incompressible jet, self-preservation analysis of the RST equations to determine the scaling of higher moments were trivial as b' is constant (George 1995). In compressible shear flows where b' scales with exponents and varies with M_c, self-preservation analysis of the RST equations provides insight into how compressibility affects the turbulence energetics. Again, introducing similarity variables for the pressure-gradient, triple-velocity correlations and dissipation gives the following equations:

$$\overline{u^i \nabla_j p''} + \overline{u^j \nabla_i p''} = \Pi_{ij}(x)\pi_{ij}(\eta), \tag{5.8}$$

$$\overline{u_i u_j u^k} = T_{ijk}(x)t_{ijk}(\eta), \tag{5.9}$$

$$-\overline{\left(\tau^{jk}\right)' \nabla_k u_i} - \overline{(\tau^{ki})' \nabla_k u_j} = E_{ij}(x)e_{ij}(\eta), \tag{5.10}$$

with $\pi_{ij}(\eta)$, $t_{ijk}(\eta)$ and $e_{ij}(\eta)$ as shape functions, and Π_{ij}, T_{ijk} and E_{ijk} as scaling functions. The scaling of the remaining turbulence moments can be determined using the scaling $R_{12} \propto U_m^2 b'$ from the mean-momentum equation (2.16). With these substitutions into the $\rho\overline{uv}$ balance from (2.5) for example, the balance with the scaling of leading-order

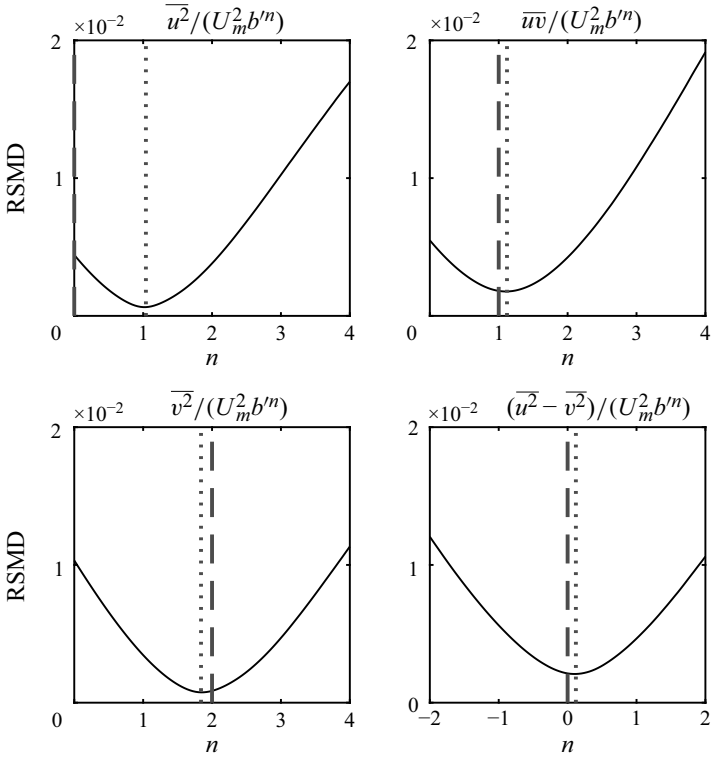

Figure 20. Error curves indicating ideal b' scaling for Reynolds stress self-preservation scaling. Minimum n (– – –) and self-preserving n (·····).

terms shown in under braces after eliminating the common factor $b/U_m^3 b'^2$,

$$0 = -\Bigg[\underbrace{\frac{\partial \rho U \overline{uv}}{\partial x} + \frac{\partial \rho V \overline{uv}}{\partial r}}_{\propto \frac{R_{12}}{U_m^2 b'}}\Bigg] - \Bigg[\underbrace{\frac{1}{r}\frac{\partial r \rho \overline{uv^2}}{\partial r}}_{\propto \frac{T_{122}}{U_m^3 b'^2}} - \underbrace{\frac{\rho \overline{uw^2}}{r}}_{\propto \frac{T_{133}}{U_m^3 b'^2}} + \underbrace{\frac{\partial \rho \overline{u^2 v}}{\partial x}}_{\propto \frac{T_{112}}{U_m^3 b'}}\Bigg]$$
$$- \Bigg[\underbrace{\overline{uv}\frac{\partial \rho V}{\partial r}}_{\propto \frac{R_{12}}{U_m^2 b'}} + \underbrace{\overline{v^2}\frac{\partial \rho U}{\partial r}}_{\propto \frac{R_{22}}{U_m^2 b'^2}} + \underbrace{\overline{u^2}\frac{\partial \rho V}{\partial x}}_{\propto \frac{R_{11}}{U_m^2}} + \underbrace{\overline{uv}\frac{\partial \rho U}{\partial x}}_{\propto \frac{R_{12}}{U_m^2 b'}}\Bigg] + \Bigg[\underbrace{\overline{p''\frac{\partial u}{\partial r}} + \overline{p''\frac{\partial v}{\partial x}}}_{\propto \frac{\Pi_{12} b}{U_m^3 b'^2}}\Bigg], \tag{5.11}$$

recalling that the pressure–diffusion, viscous–diffusion, viscous–dissipation terms and terms containing density correlations are neglected.

Using the remaining RST equations, a pattern emerges from the scaling of the remaining velocity correlations, where the power scaling of b' depends on the order and direction of the correlation. The scaling of correlations only containing streamwise components follow

$$\frac{R_{11}}{U_m^2} \propto \frac{R_{111}}{U_m^3} \propto Const., \tag{5.12}$$

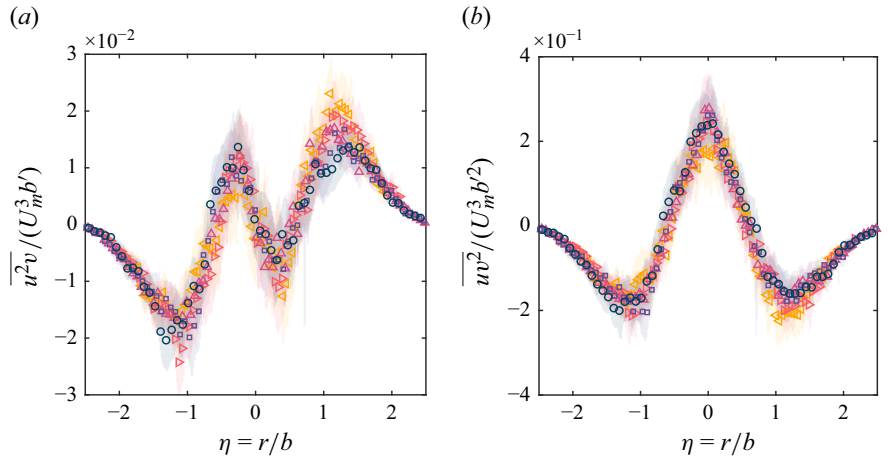

Figure 21. Similarity profiles of off-diagonal triple-velocity moments. Axial positions: $x/d = 15.0$ (○); 17.5 (□); 20.0 (△); 22.5 (◁); 25.0 (▷). Shaded areas show 95 % expanded uncertainty bounds in respective colours. (*a*) Profile collapse of u^2v with self-preservation scaling U_m^3b'; (*b*) Profile collapse of uv^2 with self-preservation scaling $U_m^3b'^2$.

a single radial or azimuthal component follow

$$\frac{R_{12}}{U_m^2} \propto \frac{R_{13}}{U_m^2} \propto \frac{R_{112}}{U_m^3} \propto \frac{R_{113}}{U_m^3} \propto b', \tag{5.13}$$

two radial or azimuthal components follow

$$\frac{R_{22}}{U_m^2} \propto \frac{R_{33}}{U_m^2} \propto \frac{R_{122}}{U_m^3} \propto \frac{R_{123}}{U_m^3} \propto \frac{R_{133}}{U_m^3} \propto b'^2, \tag{5.14}$$

and triple-moments of radial or azimuthal components follow

$$\frac{R_{222}}{U_m^3} \propto \frac{R_{223}}{U_m^3} \propto \frac{R_{233}}{U_m^3} \propto \frac{R_{333}}{U_m^3} \propto b'^3. \tag{5.15}$$

For Cartesian flows, analogous scalings are observed, where the azimuthal component is instead the spanwise component. In the previous section where the Reynolds stresses were compared with experimental data, the scaling of R_{12} and R_{22} appeared consistent with (5.13) and (5.14), respectively. The scaling of R_{11} was to be $\propto U_m^2b'$ and was found not to scale as per (5.12), and instead appears to be constrained by (5.5). Although not exact, these findings provide a framework for the scaling of velocity correlations in compressible shear flows. In the following section, the scalings are applied to and compared with the triple-velocity correlation jet data.

5.6. *Self-preservation scaling of the triple-velocity correlations*

The compressibility scaling can be extended to the triple-velocity correlations, where profiles are also observed with the compressible jet data. Figures 21(*a*) and 21(*b*) present the triple-velocity correlations, $\overline{u^2v}$ and $\overline{uv^2}$, respectively, normalised using their corresponding self-preservation scaling. By normalising with the appropriate power of the spreading rate, b', the profiles for $\overline{u^2v}$ and $\overline{uv^2}$ collapse onto a single curve. Demonstrating that the scaling derived from the self-preservation analysis can be successfully extended to the RST equations and applied to higher-order velocity moments.

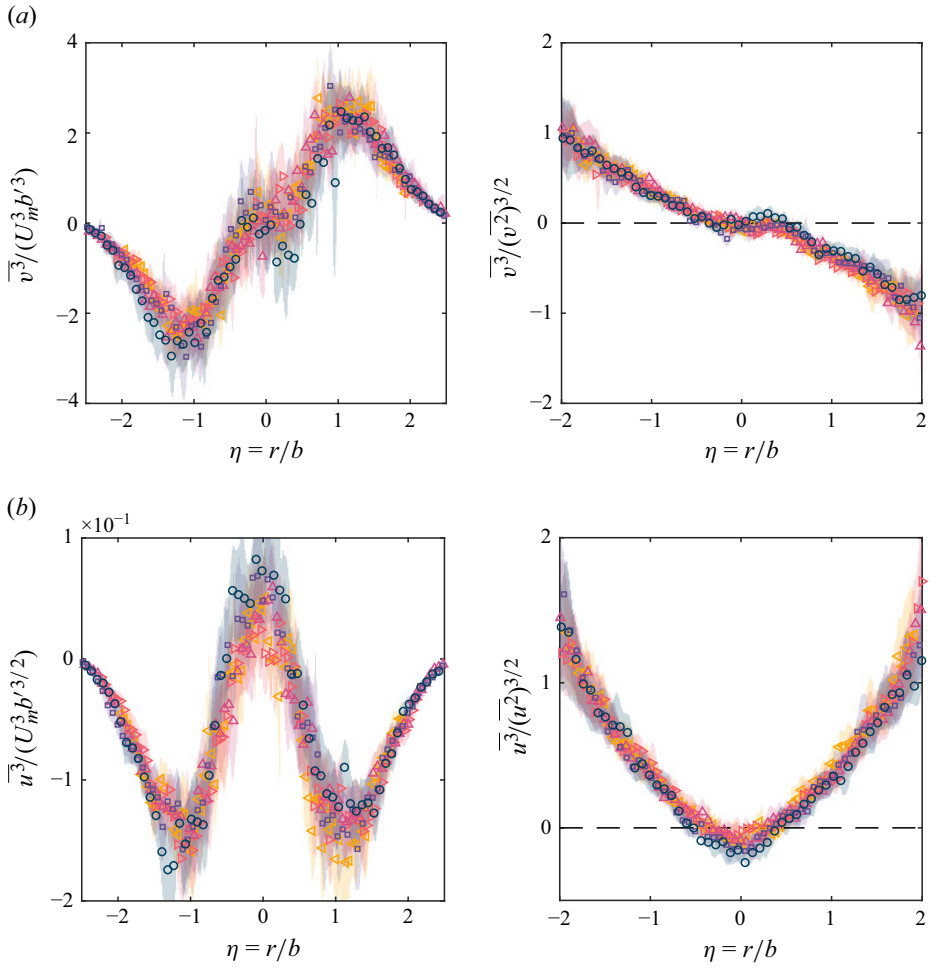

Figure 22. Profiles of normal triple-velocity correlations and skewness. Axial positions: $x/d = 15.0$ (○); 17.5 (□); 20.0 (△); 21.5 (◁); 25.0 (▷). Shaded areas show 95 % expanded uncertainty bounds in respective colours. (*a*) Profile collapse of $\overline{v^3}$ with self-preservation scaling $U_m^3 b'^3$; (*b*) Profile collapse of $\overline{u^3}$ with scaling $U_m^3 b'^{3/2}$.

Figure 22(*a*) presents the profiles of $\overline{v^3}$, which collapse effectively when normalised using the self-preservation scaling $U_m^3 b'^3$. This collapse indicates that the self-preservation scaling applies well to the triple-velocity moments in the jet. Profiles of the skewness of v are also shown, showing collapse and consistency of the compressible scaling of the v-velocity fluctuations with M_c. Rotational symmetry, where $v = w$, also confirms the scaling for $\overline{w^2}$ and $\overline{uw^2}$ moments on the jet centreline. The agreement of the scaling for these moments further supports the applicability of the similarity analysis for higher-order velocity moments in compressible jets.

Similar to $\overline{u^2}$, the self-preservation scaling does not yield self-similar profiles for $\overline{u^3}$. However, as shown in figure 22(*b*), $\overline{u^3}$ scales with $b'^{3/2}$, consistent with the scaling found for $\overline{u^2}$ where $u \propto b'^{1/2}$. This scaling indicates that neither $\overline{u^2}$ nor $\overline{u^3}$ follows the scaling under the similarity assumption, but scale at least consistently. The skewness of u also

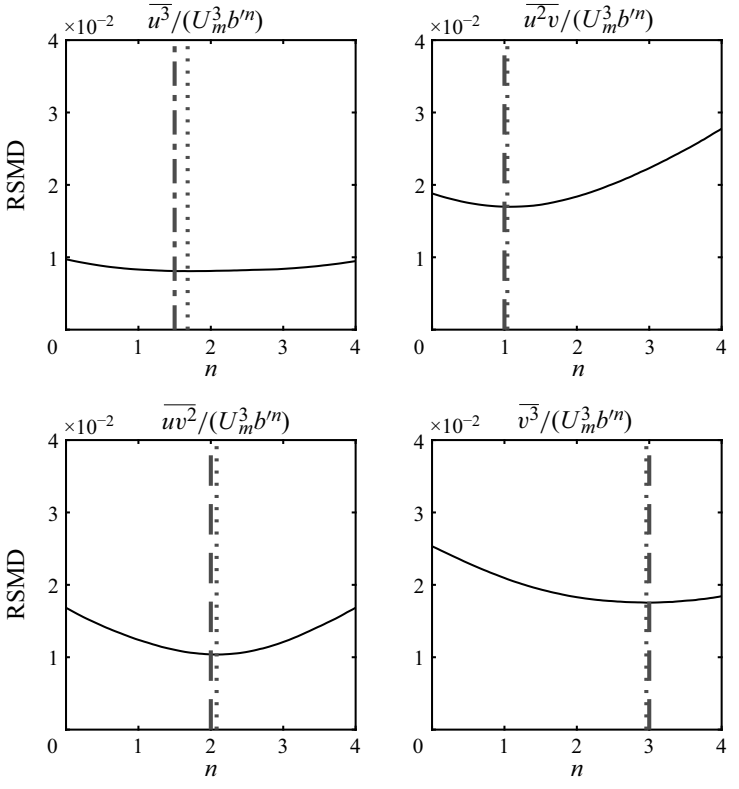

Figure 23. Error curves indicating ideal b' scaling for triple-velocity correlations self-preservation scaling. Minimum n (·····) and self-preserving n (– – –).

exhibits self-similar profiles across the jet for all Mach numbers. The consistent scaling behaviour, along with the skewness similarity, points to an underlying structure in the velocity field that is preserved across different flow Mach numbers.

Figure 23 shows the error curves concerning the similarity of the triple-velocity correlation data for the Mach 1.25 jet using the method introduced in § 5.4. When compared with the error curves for Reynolds stresses shown previously in figure 20, the curves for the triple-velocity correlations exhibit a smaller depression due to increased scatter in the data. Despite this, the minimum RMSD for the profiles aligns with the self-preservation scaling for $\overline{u^2v}$, $\overline{uv^2}$ and $\overline{v^3}$. As discussed, $\overline{u^3}$ instead scales to the b' exponent $(3/2)$, such that the scale is consistent with $\overline{u^2}$. The consistency of the scaling results between double- and triple-velocity moments increases confidence in the application of self-preservation principles in analysing compressible shear flows.

6. Reynolds-stress-transport budgets

Having established the scaling of the triple-velocity correlations, the scaling of the remaining Reynolds-stress-transport terms in (2.5), expanded in Appendix B, are considered. Since b' varies with x, the scaling is first confirmed. Next, pressure appears to play a significant role in both the self-preservation, as previously observed in the Reynolds-normal stresses in § 5.2, as well as a mechanism in the attenuation of turbulence in compressible shear flows through the pressure strain.

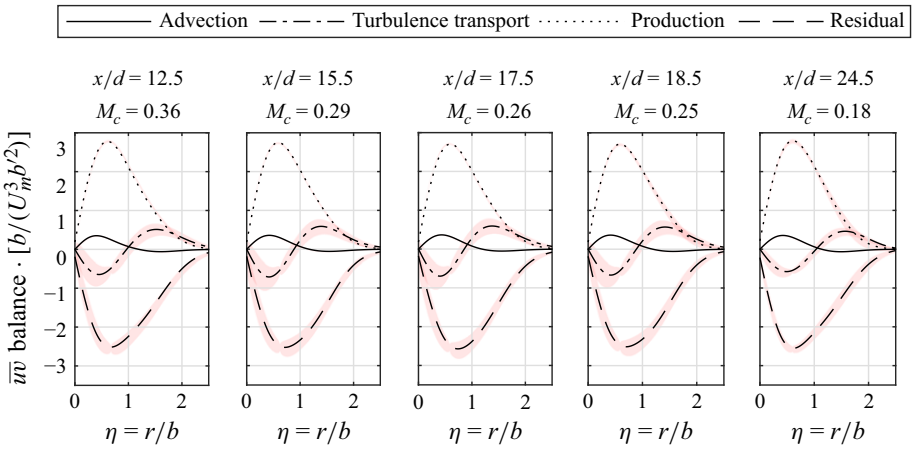

Figure 24. Normalised budget of $\overline{uv}$. Red shaded areas show 95 % expanded uncertainty bounds.

6.1. *Turbulence energetics*

From the velocimetry data, the advection, turbulence-transport and production terms can be calculated directly. Therefore, the pressure–strain, dissipation, molecular–diffusion and pressure–diffusion terms are lumped as the residual of the equation. For high-Re shear flows, the effect of molecular diffusion is negligible and pressure diffusion generally small. To mitigate the effect due to random noise and to ensure differentiability, the turbulence moments are curve-fitted, with radial distributions as reported by Hussein *et al.* (1994), and streamwise distributions fitted with low-order polynomials. The balances are then calculated using the fitted functions, where the fit uncertainties are propagated to indicate 95 % expanded confidence bounds in shaded areas.

The Reynolds transport equations are presented with the common factor $b/U_m^3 b'^n$, where n is a power determined previously through self-preservation analysis. The balance of the $\overline{uv}$ transport equation is shown in figure 24, where the common factor is $b/U_m^3 b'^2$. The balances scale producing profiles of similar magnitude, implying they are independent of M_c after normalisation. Note that $\overline{uv^2}$ is used to approximate $\overline{uw^2}$ since w data are unavailable. For high-Re incompressible jets, the Richardson–Kolmogorov–Onsager theory implies a separation of scales where dissipation, which occurs at the small scales, exhibits scale locality. While compressible turbulence superficially resembles the incompressible cascade, the exact inter-scale energy dynamics remains unclear, but analysis from Aluie (2011) has shown scale locality and the existence of an inertial range in compressible flows. This suggests dissipation can be approximated as isotropic and the off-diagonal components of dissipation neglected, especially for this flow where density effects are moderate. Therefore, the residual terms in the $\overline{uv}$ transport equation approximate the pressure–strain component. With the primary source term production, the major sink term is the pressure strain, indicating turbulent kinetic energy is being redistributed to the other stress balances. Note, the shear pressure–strain component scales proportionally to the component production, agreeing with observations from Matsuno & Lele (2020). As $\overline{uv}$ is the dominating term, which spreads the jet through the streamwise momentum equation (2.13), it is unsurprising that the balance shows self-preservation.

The budget of $\overline{v^2}$ is shown in figure 25 normalised by $b/U_m^3 b'^3$. Here, $\overline{vw^2}$ is substituted by $\overline{v^3}$. Compared with setting $\overline{vw^2} = 0$, the magnitude of the turbulence–diffusion term changes less than 10 %. This substitution was also made by Hussein *et al.* (1994) when

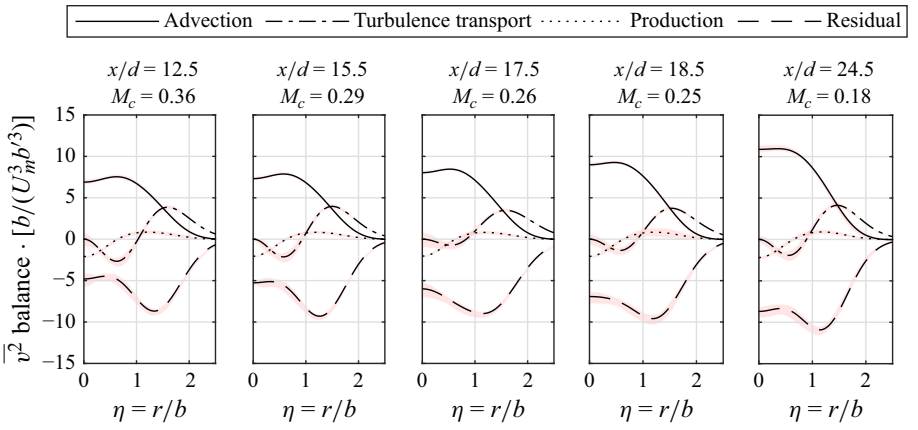

Figure 25. Normalised budget of $\overline{v^2}$. Red shaded areas show 95 % expanded uncertainty bounds.

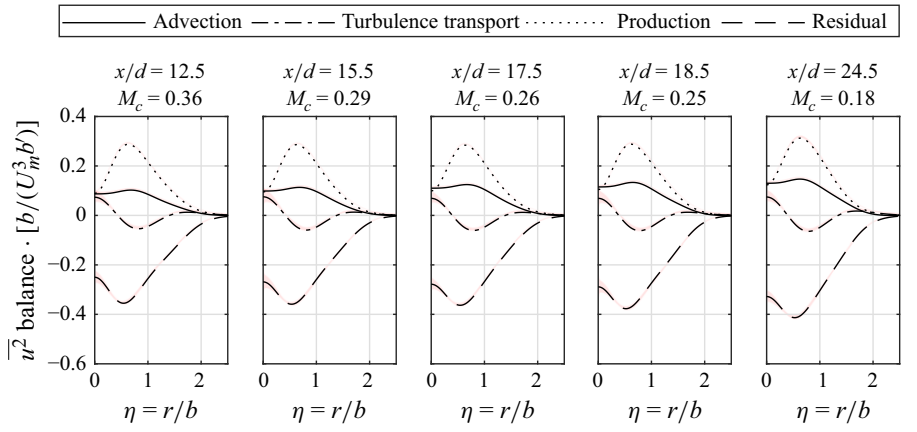

Figure 26. Normalised budget of $\overline{u^2}$. Red shaded areas show 95 % expanded uncertainty bounds.

lacking w information and suggested that approximating $\overline{vw^2}$ with $\overline{v^3}$ is satisfactory for estimating the scaling behaviour of the residual of the $\overline{v^2}$-transport equation. The balance of $\overline{v^2}$ is difficult to interpret by itself, as the major source term is the pressure–strain term and the major sink term is the dissipation (Hussein *et al.* 1994). With the present data, while $\overline{v^2}$ was shown to be self-similar when scaled by the self-preserving scaling $U_m^3 b'^2$, the advection terms are not. The turbulence-transport and production terms appear self-similar, while the residual terms containing the dissipation and pressure strain is not self-preserving and balances the scaling of the advection.

In the budget of $\overline{u^2}$, shown in (B1), the terms share a common factor of $b/U_m^3 b'$, which has been applied to the $\overline{u^2}$ balance across various M_c, as shown in figure 26. In the $\overline{u^2}$ budget, the primary source term is the production and advection terms. This turbulent kinetic energy is then transported into the $\overline{v^2}$ equation and contributes to the production of $\overline{uv}$. Therefore, limited production of $\overline{u^2}$ due to M_c is suggested to play a role in the reduced spreading rate. The production and turbulence transport terms appear to be self-preserving at all M_c; meanwhile, the advection terms increase as M_c decreases. The situation in the

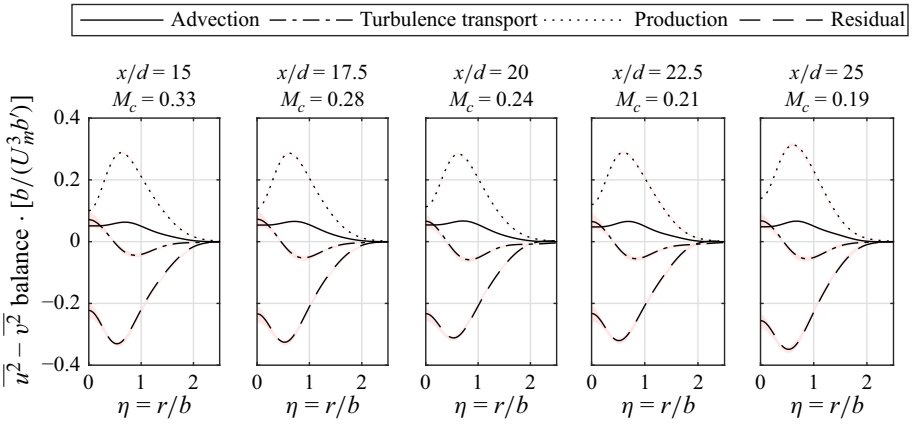

Figure 27. Normalised budget of $\overline{u^2} - \overline{v^2}$. Red shaded areas show 95 % expanded uncertainty bounds.

$\overline{u^2}$ balance is similar to the $\overline{v^2}$ balance – profiles of advection are not self-similar, and a similar imbalance is observed in the residual. As the residual of the balance contains the pressure–strain term and dissipation term, the pressure strain is responsible for transferring energy to the $\overline{v^2}$ budget. Although the terms in the budgets of $\overline{u^2}$ and $\overline{v^2}$ do not conveniently collapse, a strong coupling is observed between these equations, which is already evident in the momentum equation (5.4) where the collapse of the difference $\overline{u^2} - \overline{v^2}$ collapses with U_m^2, as seen previously in figure 17.

Figure 27 shows the difference between budgets (B1) and (B2) normalised by $b/U_m^3 b'$; remarkably, the profiles are observed to be self-preserving. The balance of the difference resembles the balance of $\overline{u^2}$, where the turbulence production and then advection are the significant source terms. The scaling of the advection terms previously observed in the individual $\overline{u^2}$ and $\overline{v^2}$ balances appear to redistribute energy to each other such that the resulting advection of the difference is self-preserving. As a result, the residual of the difference scales is self-preserving. Closer consideration of the residual term for the difference balance, (B1)–(B2), yields further insight. An isotropic dissipation model implies that the contributor of dissipation in the residual term vanishes. In contrast, the pressure–strain terms between axial and radial directions tend to differ in sign. Hence, the residual term is dominated by the redistribution due to the pressure strain. This observation shows the importance of the pressure–strain redistribution in the coupling of $\overline{u^2}$ and $\overline{v^2}$, and the internal dynamics leading to self-preservation and role in the attenuation of energy redistribution.

Figure 28(*a*) plots the pressure–strain component Π_{12} estimated from the residual of the $\overline{uv}$ balance as a function of M_c. The pressure strain is normalised by its incompressible value, estimated from the furthest value available downstream. From the self-preservation analysis of the $\overline{uv}$ balance, Π_{12} scales with $b/U_m^3 b'^2$. Compared with mixing layer data from Pantano & Sarkar (2002), significant attenuation of the pressure–strain component is observed, verifying the behaviour of the shear pressure strain. From the current jet data, individual normal pressure–strain components cannot be calculated. Instead, from the balance of the difference between the $\overline{u^2}$ and $\overline{v^2}$ equations, the residual scales with $b/U_m^3 b'$. Again, this residual is approximately $\Pi_{11} - \Pi_{22}$, assuming isotropic turbulence where the diagonal dissipation terms are of similar magnitude. Note that Π_{11} and Π_{22} are expected to have opposite signs, such that their differences increase their contribution

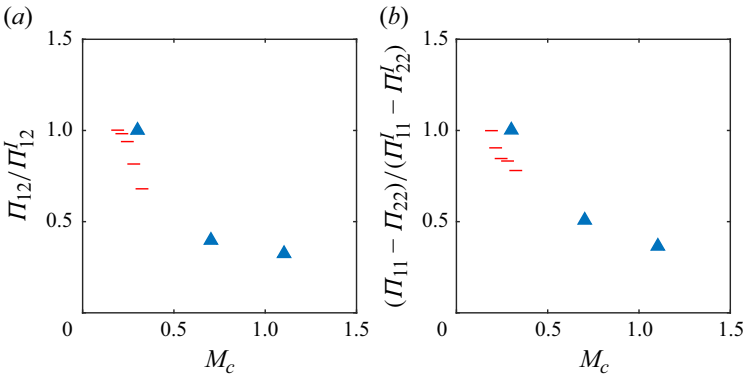

Figure 28. Pressure–strain components normalised by incompressible value as a function of M_c for the mixing layer (Pantano & Sarkar 2002) (▲) and the current jet (-). (*a*) Normalised Π_{12}; (*b*) normalised Π_{12}–Π_{22} estimated from (B1) - (B2).

to the $\overline{u^2}-\overline{v^2}$ transport balance. Figure 28(*b*) plots the normal pressure–strain terms, normalised by b/U_m^3, which appears to be attenuated by M_c through b', again agrees with the scaling observed in the mixing layer. Note that the off-diagonal term appears to scale to different powers of b' than the diagonal terms; this difference in scaling was also exhibited in the mixing layer data of Pantano & Sarkar (2002). This indicates that pressure modification is consistent with the self-preservation scaling framework in the current jet study and directly connected to the reduced spreading rates due to increasing M_c.

7. Summary and conclusion

High-speed PIV measurements were conducted for subsonic ($M_{jet}=0.3$) and supersonic ($M_{jet}=1.25$) perfectly expanded jets. The supersonic jet conditions were limited to ensure density-fluctuation correlations remained small. For the $M_{jet}=1.25$ jet, b' was attenuated as M_c increases, showing a similar trend to the compressible mixing layer. This behaviour indicates that the attenuation of turbulence behaves similarly across free compressible shear flows. However, when comparing the attenuation function $\Phi(M_c)$, which describes the relationship between b' and M_c, the axisymmetric jet is more closely aligned with axisymmetric mixing layer experiments. This behaviour suggests that factors such as geometry influence the behaviour of the attenuation.

By applying the current self-preservation theory and expanding on observations from compressible mixing layers, turbulence moments were found to scale as functions of powers of b'. Due to the behaviour of the Reynolds-stress-transport equations, the power of b' depends on the component and the order of the moment, with some moments exhibiting more substantial attenuation than others. These findings are notable given the discrepancies and scatter previously reported in Reynolds stresses and provide direction into the behaviour of Reynolds-stress anisotropy.

It is found that the intensity of the attenuation of component velocity moments can be predicted and is consistent with self-preservation. Velocity moments containing radial or azimuthal components scale according to self-preservation analysis as the velocity moments scale with powers of b' for each radial or azimuthal component. For example, in the $M_{jet}=1.25$ case, $\overline{uv}\propto U_m^2 b'$, $\overline{v^2}\propto U_m^2 b'^2$, $\overline{v^3}\propto U_m^2 b'^3$ and so on. Velocity moments containing explicitly streamwise components were attenuated, where $\overline{u^2}\propto U_m^2 b'$ and $\overline{u^3}\propto U_m^2 b'^{3/2}$. These scalings remain consistent with self-preservation of the mean momentum

equation, where after substituting the pressure term for $\overline{v^2}$, the Reynolds-normal-stress difference, $\overline{u^2} - \overline{v^2}$, exhibits collapsed profiles when normalised by U_m^2. The behaviour of the Reynolds stresses suggest self-preservation is observed despite Mach number effects and that pressure plays a role in the scaling of $\overline{u^2}$.

When examining the Reynolds-stress-transport equations, the self-preservation scalings were also applicable. For $M_{jet} = 1.25$, the collapse of all terms in the $\overline{uv}$ budget after normalisation indicates that self-preservation extends to turbulence energetics. Collapsed profiles were also observed when considering the budget of the Reynolds-normal-stress difference, which indicates internal regulation of energy occurs within the normal stresses, influencing the redistribution due to pressure strain. Each component was also attenuated and scaled with powers of b', and attributed as the source of turbulence attenuation due to compressibility. The shear component of pressure strain, Π_{12}, was found to scale $\propto U_m^3 b'^2/b$, meanwhile, $\Pi_{11} - \Pi_{22} \propto U_m^3 b'/b$. The consistency observed in the scalings of the pressure strain and other turbulence moments suggests that compressible turbulence is orderly and can be used to redefine two-point closure models capturing these compressibility effects. The behaviour at higher Mach numbers and different geometries remains to be established, as well as identifying the underlying further physics responsible for the reduction in energetic redistribution due to the attenuated pressure strain observed.

Funding. Funding for this work was provided by the Natural Sciences Engineering Research Council (NSERC) of Canada and Atlantis Research Labs Inc. through a Collaborative Research and Development (CRD) grant.

Declaration of interests. The authors report no conflict of interest.

Appendix A. Compressible Reynolds-stress-transport equations

In compressible shear flows, the transport equations are commonly expressed using Favre averaging (Knight 1997). As a consequence of strong Reynolds analogy, turbulence moments using Reynolds or Favre averaging are approximately similar under the restrictions from (2.1), for example, $\overline{uv} \approx \widetilde{uv}$, where $\widetilde{uv}$ is the Favre-averaged Reynolds stress. For further information on the differences between the averaging procedures, see Knight (1997).

For reference, the continuity, momentum and Reynolds-stress-transport equations using conventional Reynolds averaging is shown respectively as

$$\frac{\partial \rho}{\partial t} + \nabla_i\left(\rho \overline{U}^i\right) = -\nabla_i\left(\overline{\rho'' u^i}\right), \tag{A1}$$

$$\rho \frac{\partial U_i}{\partial t} + \rho U^j \nabla_j U_i = \nabla_i \overline{p} + \nabla_j \overline{\tau}_i^j - \nabla_j\left(\rho \overline{u_i u^j}\right) - \overline{U}^j \nabla_j\left(\overline{\rho'' u_i}\right) - \overline{\rho'' u^j} \nabla_j U_i - \nabla_j\left(\overline{\rho'' u^j u_i}\right) - \frac{\partial}{\partial t}\left(\overline{\rho'' u_i}\right), \tag{A2}$$

$$\underbrace{\frac{\partial \rho \overline{u_i u_j}}{\partial t} + \nabla_k\left(U^k \rho \overline{u_i u_j}\right)}_{\text{advection}} = \underbrace{-\frac{\partial U_i}{\partial t}\overline{\rho'' u_j} - \overline{\rho'' u_i}\frac{\partial U_j}{\partial t} - \frac{\partial \overline{\rho'' u_i u_j}}{\partial t}}_{\text{unsteady-fluctuating-density correlations}}$$

$$- \nabla_k\Bigg[\underbrace{\rho \overline{u^k u_i u_j}}_{\substack{\text{turbulent}\\ \text{diffusion}}} + \underbrace{U^k \overline{\rho'' u_i u_j} + \overline{\rho'' u^k u_i u_j}}_{\substack{\text{fluctuating-}\\ \text{density diffusion}}} - \underbrace{\overline{u_i p''}\delta_j^k - \overline{u_j p''}\delta_i^k}_{\text{pressure diffusion}} - \underbrace{\overline{u_i\left(\tau_j^k\right)''} - \overline{u_j\left(\tau_i^k\right)''}}_{\text{viscous diffusion}}\Bigg]$$

$$\underbrace{-\left(\rho\overline{u_j u^k}+\overline{\rho'' u_j}U^k+\overline{\rho'' u^j u^k}\right)\nabla_k U_i-\left(\rho\overline{u_i u^k}+\overline{\rho'' u_i}U^k+\overline{\rho'' u_i u^k}\right)\nabla_k U_j}_{\text{production}}$$
$$+\underbrace{\left[\overline{p''\nabla_j u_i}+\overline{p''\nabla_i u_j}\right]}_{\text{pressure strain}}-\underbrace{\left[\overline{\left(\tau_j^k\right)''\nabla_k u_i}+\overline{\left(\tau_i^k\right)''\nabla_k u_j}\right]}_{\text{viscous dissipation}}. \tag{A3}$$

As seen, double and triple moments containing density-fluctuations are introduced from the Reynolds-averaging operation. Neglecting the density-fluctuating moments as per (2.1), unsteady pressure–diffusion and viscous–diffusion terms result in the simplified set of equations shown in (2.5).

Appendix B. Self-preservation of the RST equations

After reducing the RST equations to only include terms up to the first order, as performed in § 2.1, the reduced RST budgets are provided where the behaviour of the scaling functions is made explicit. The scaling functions for each individual term are shown after removing a common factor in under braces. Here, ϵ denotes the viscous dissipation terms.

The $\overline{\rho u^2}$ balance with common factor $b/U_m^3 b'$ removed is

$$0=\underbrace{\left[\frac{\partial\rho U\overline{u^2}}{\partial x}+\frac{\partial\rho V\overline{u^2}}{\partial r}\right]}_{\propto\frac{R_{11}}{U_m^2}\propto\frac{(R_{11})'}{U_m^2 b'}}-\left[\underbrace{\frac{1}{r}\frac{\partial r\rho\overline{u^2 v}}{\partial r}}_{\propto\frac{T_{112}}{U_m^3 b'}}-\underbrace{\frac{\partial\rho\overline{u^3}}{\partial x}}_{\propto\frac{T_{111}}{U_m^3}}\right]$$
$$-\left[\underbrace{2\overline{uv}\frac{\partial\rho U}{\partial r}}_{\propto\frac{R_{12}}{U_m^2 b'}}+\underbrace{2\overline{u^2}\frac{\partial\rho U}{\partial x}}_{\propto\frac{R_{11}}{U_m^2}}\right]+\left[\underbrace{2\overline{p''\frac{\partial u}{\partial x}}}_{\propto\frac{\Pi_{11}b}{U_m^3 b'}}\right]-2\epsilon_{11}. \tag{B1}$$

The $\overline{\rho v^2}$ balance with common factor $b/U_m^3 b'^3$ removed is

$$0=\underbrace{\left[\frac{\partial\rho U\overline{v^2}}{\partial x}+\frac{\partial\rho V\overline{v^2}}{\partial r}\right]}_{\propto\frac{R_{22}}{U_m^2 b'}\propto\frac{(R_{22})'}{U_m^2 b'^2}}-\left[\underbrace{\frac{1}{r}\frac{\partial r\rho\overline{v^3}}{\partial r}}_{\propto\frac{T_{222}}{U_m^3 b'^3}}-\underbrace{2\frac{\rho\overline{vw^2}}{r}}_{\propto\frac{T_{233}}{U_m^3 b'^3}}+\underbrace{\frac{\partial\rho\overline{uv^2}}{\partial x}}_{\propto\frac{T_{122}}{U_m^2 b'^2}}\right]$$
$$-\left[\underbrace{2\overline{v^2}\frac{\partial\rho V}{\partial r}}_{\propto\frac{R_{22}}{U_m^2 b'^2}}+\underbrace{2\overline{uv}\frac{\partial\rho V}{\partial x}}_{\propto\frac{R_{12}}{U_m^2 b'}}\right]+\left[\underbrace{2\overline{p''\frac{\partial v}{\partial r}}}_{\propto\frac{\Pi_{22}b}{U_m^3 b'^3}}\right]-2\epsilon_{22}. \tag{B2}$$

The $\overline{\rho w^2}$ balance with common factor $b/U_m^3 b'^3$ removed is

$$0 = \Bigg[\underbrace{\frac{\partial}{\partial x}\left(\rho U\overline{w^2}\right) + \frac{\partial}{\partial r}\left(\rho V\overline{w^2}\right)}_{\propto \frac{R_{33}}{U_m^2 b'^2} \propto \frac{(R_{33})'}{U_m^2 b'^2}}\Bigg] - \Bigg[\underbrace{\frac{1}{r}\frac{\partial}{\partial r}\left(r\rho\overline{vw^2}\right)}_{\propto \frac{T_{233}}{U_m^3 b'^3}} - \underbrace{2\frac{\rho\overline{vw^2}}{r}}_{\propto \frac{T_{233}}{U_m^3 b'^3}} + \underbrace{\frac{\partial}{\partial x}\left(\rho\overline{uw^2}\right)}_{\propto \frac{T_{133}}{U_m^3 b'^2}}\Bigg]$$
$$- \Bigg[\underbrace{2\rho\overline{w^2}\frac{V}{r}}_{\propto \frac{R_{33}}{U_m^2 b'^2}}\Bigg] + \Bigg[\underbrace{2\overline{p''\frac{\partial w}{\partial \theta}}}_{\propto \frac{\Pi_{33} b}{U_m^3 b'^3}}\Bigg] - 2\epsilon_{33}. \tag{B3}$$

References

Aluie, H. 2011 Compressible turbulence: the cascade and its locality. *Phys. Rev. Lett.* **106** (17), 174502.

Barre, S., Quine, C. & Dussauge, J.P. 1994 Compressibility effects on the structure of supersonic mixing layers: experimental results. *J. Fluid Mech.* **259**, 47–78.

Benedict, L.H. & Gould, R.D. 1996 Towards better uncertainty estimates for turbulence statistics. *Exp. Fluids* **22** (2), 129–136.

Bogdanoff, D.W. 1983 Compressibility effects in turbulent shear layers. *AIAA J.* **21** (6), 926–927.

Bradbury, L.J.S. & Riley, J. 1967 The spread of a turbulent plane jet issuing into a parallel moving airstream. *J. Fluid Mech.* **27** (2), 381–394.

Bradshaw, P. 1977 Compressible turbulent shear layers. *Annu. Rev. Fluid Mech.* **9** (1), 33–52.

Brown, G.L. & Roshko, A. 1974 On density effects and large structure in turbulent mixing layers. *J. Fluid Mech.* **64** (4), 775–816.

Chinzei, N., Masuya, G., Komuro, T., Murakami, A. & Kudou, K. 1986 Spreading of two-stream supersonic turbulent mixing layers. *Phys. Fluids* **29** (5), 1345.

Clemens, N.T. & Mungal, M.G. 1995 Large-scale structure and entrainment in the supersonic mixing layer. *J. Fluid Mech.* **284**, 171–216.

Debisschop, J.R., Chambers, O. & Bonnet, J.P. 1994 Velocity field characteristics in supersonic mixing layers. *Expl Therm. Fluid Sci.* **9** (2), 147–155.

Dimotakis, P.E. 1991 *Turbulent Free Shear Layer Mixing and Combustion, High Speed Flight Propulsion Systems, in Progress in Astronautics and Aeronautics 137*, Ch. 5, pp. 265–340.

Elliott, G.S. & Samimy, M. 1990 Compressibility effects in free shear layers. *Phy. Fluids A: Fluid Dyn.* **2** (7), 1231–1240.

Feng, T. & McGuirk, J.J. 2016 Measurements in the annular shear layer of high subsonic and under-expanded round jets. *Exp. Fluids* **57** (1), 7.

Ferri, A., Libby, P.A. & Zakkay, V. 1964 Theoretical and experimental investigation of supersonic combustion. In *High Temperatures in Aeronautics*, pp. 55–118. Elsevier.

Freund, J.B., Lele, S.K. & Moin, P. 2000 Compressibility effects in a turbulent annular mixing layer. Part 1. Turbulence and growth rate. *J. Fluid Mech.* **421**, 229–267.

George, W.K. 1989 The self-preservation of turbulent flows and its relation to initial conditions and coherent structures. In *Advances in Turbulence* (ed. W.K. George & R.E.A. Arndt), pp. 39–72. Hemisphere.

George, W.K. 1995 Some new ideas on the similarity of the turbulent free shear flows. In *Turbulence, Heat and Mass Transfer 1*. Begell House.

Goebel, S.G. & Dutton, J.C. 1991 Experimental study of compressible turbulent mixing layers. *AIAA J.* **29** (4), 538–546.

Gutmark, E. 1983 Preferred modes and the spreading rates of jets. *Phys. Fluids* **26** (10), 2932.

Hussein, H.J., Capp, S.P. & George, W.K. 1994 Velocity measurements in a high-Reynolds-number, momentum-conserving, axisymmetric. *J. Fluid Mech.* **258**, 31–75.

Kleinstein, G. 1964 Mixing in turbulent axially symmetric free jets. *J. Spacecr. Rockets* **1** (4), 403–408.

Kline, S.J., Cantwell, B.J. & Lilley, G.M. 1982, Proc. 1980-810-AFOSR-HTTM-stanford conference on turbulent flows: comparison of computational and experiment. Tech. Rep. AFOSR-TR 82-0371. Stanford University.

Knight, D.D. 1997 Numerical simulation of compressible turbulent flows using the Reynolds-averaged Navier–Stokes equations. In *Turbulence in Compressible Flows*. AGARD.

LAU, J.C. 1981 Effects of exit Mach number and temperature on mean-flow and turbulence characteristics in round jets. *J. Fluid Mech.* **105**, 193.

LAU, J.C., MORRIS, P.J. & FISHER, M.J. 1979 Measurements in subsonic and supersonic free jets using a laser velocimeter. *J. Fluid Mech.* **93** (1), 1–27.

LELE, S.K. 2021 Turbulence in compressible flows. In *Advanced Approaches in Turbulence*, pp. 399–481. Elsevier.

MATSUNO, K. & LELE, S.K. 2020 Compressibility effects in high speed turbulent shear layers – revisited. In *AIAA Scitech 2020 Forum*. American Institute of Aeronautics and Astronautics.

MENAA, M. 2003 Density and compressibility effects on the structure of supersonic mixing layer. In *12th AIAA International Space Planes and Hypersonic Systems and Technologies*. American Institute of Aeronautics and Astronautics.

MORKOVIN, M.V. 1964 Effects of compressibility of turbulent flows. In *The Mechanics of Turbulence*, pp. 367–380. Gordon and Breach.

NGUYEN, C.T. & OBERLACK, M. 2024 Analysis of a turbulent round jet based on direct numerical simulation data at large box and high Reynolds number. *Phys. Rev. Fluids* **9** (7), 074608.

PANTANO, C. & SARKAR, S. 2002 A study of compressibility effects in the high-speed turbulent shear layer using direct simulation. *J. Fluid Mech.* **451**, 329–371.

PAPAMOSCHOU, D. & ROSHKO, A. 1988 The compressible turbulent shear layer: an experimental study. *J. Fluid Mech.* **197**, 453–477.

RAGNI, D., SCHRIJER, F., VAN OUDHEUSDEN, B.W. & SCARANO, F. 2011 Particle tracer response across shocks measured by PIV. *Exp. Fluids* **50** (1), 53–64.

SAMIMY, M. & ELLIOTT, G.S. 1990 Effects of compressibility on the characteristics of free shear layers. *AIAA J.* **28** (3), 439–445.

SARKAR, S. & BALAKRISHNAN, L. 1990 Application of a Reynolds Stress Turbulence Model to the Compressible Shear Layer. In *21st Fluid Dynamics, Plasma Dynamics and Lasers Conference*, American Institute of Aeronautics and Astronautics.

SCARANO, F. 2008 Overview of PIV in supersonic flows. In *Particle Image Velocimetry*, vol. 112, pp. 445–463, Springer, Topics in Applied Physics.

SMITS, A.J. & DUSSAUGE, J.-P. 2006 *Turbulent Shear Layers in Supersonic Flow*. 2nd edn. Springer.

TAM, C.K.W. 1995 Supersonic jet noise. *Annu. Rev. Fluid Mech.* **27**, 17–43.

TOWNSEND, A.A. 1980 *The Structure of Turbulent Shear Flow*. 2nd edn. Cambridge University Press.

URBAN, W.D. & MUNGAL, M.G. 2001 Planar velocity measurements in compressible mixing layers. *J. Fluid Mech.* **431**, 34.

VREMAN, A.W., SANDHAM, N.D. & LUO, K.H. 1996 Compressible mixing layer growth rate and turbulence characteristics. *J. Fluid Mech.* **320**, 235.

WERNET, M.P. 2016 Application of Tomo-PIV in a large-scale supersonic jet flow facility. *Exp. Fluids* **57** (9), 144.

WILCOX, D.C. 1992 Dilatation-dissipation corrections for advanced turbulence models. *AIAA J.* **30** (11), 2639–2646.

WITZE, P.O. 1974 Centerline velocity decay of compressible free jets. *AIAA J.* **12** (4), 417–418.

WYGNANSKI, I. & FIEDLER, H. 1969 Some measurements in the self-preserving jet. *J. Fluid Mech.* **38** (3), 577–612.

ZHANG, D., TAN, J. & YAO, X. 2019 Direct numerical simulation of spatially developing highly compressible mixing layer: structural evolution and turbulent statistics. *Phys. Fluids* **31** (3), 036102.